Contents lists available at ScienceDirect

Remote Sensing of Environment

Detection of vegetation drying signals using diurnal variation of land surface temperature: Application to the 2018 East Asia heatwave

Yuhei Yamamoto [a,b,*], Kazuhito Ichii [b], Youngryel Ryu [c], Minseok Kang [d], Shohei Murayama [e], Su-Jin Kim [f], Jamie R. Cleverly [g]

[a] *Institute for Advanced Academic Research (IAAR), Chiba University, 1-33, Yayoi-cho, Inage-ku, Chiba, 263-8522, Japan*
[b] *Center for Environmental Remote Sensing (CEReS), Chiba University, 1-33, Yayoi-cho, Inage-ku, Chiba 263-8522, Japan*
[c] *Department of Landscape Architecture and Rural Systems Engineering, Seoul National University, 1, Gwanak-ro, Gwanak-gu, Seoul 08826, Republic of Korea*
[d] *National Center for AgroMeteorology, 1, Gwanak-ro, Gwanak-gu, Seoul 08826, Republic of Korea*
[e] *National Institute of Advanced Industrial Science and Technology (AIST), AIST Tsukuba West 16-1, Onogawa, Tsukuba, Ibaraki 305-8569, Japan*
[f] *National Institute of Forest Science, 57, Hoegi-ro, Dongdaemun-gu, Seoul 02455, Republic of Korea*
[g] *College of Science and Engineering, James Cook University, Cairns, Queensland, Australia*

ARTICLE INFO

ABSTRACT

Satellite-based vegetation monitoring provides important insights regarding spatiotemporal variations in vegetation growth from a regional to continental scale. Most current vegetation monitoring methodologies rely on spectral vegetation indices (VIs) observed by polar-orbiting satellites, which provide one or a few observations per day. This study proposes a new methodology based on diurnal changes in land surface temperatures (LSTs) using Japan's geostationary satellite, Himawari-8/Advanced Himawari Imager (AHI). AHI thermal infrared observation provides LSTs at 10-min frequencies and ~ 2 km spatial resolution. The DTC parameters that summarize the diurnal cycle waveform were obtained by fitting a diurnal temperature cycle (DTC) model to the time-series LST information for each day. To clarify the applicability of DTC parameters in detecting vegetation drying under humid climates, DTC parameters from in situ LSTs observed at vegetation sites, as well as those from Himawari-8 LSTs, were evaluated for East Asia. Utilizing the record-breaking heat wave that occurred in East Asia in 2018 as a case study, the anomalies of DTC parameters from the Himawari-8 LSTs were compared with the drying signals indicated by VIs, latent heat fluxes (LE), and surface soil moisture (SM). The results of site-based and satellite-based analyses revealed that DTR (diurnal temperature range) correlates with the evaporative fraction (EF) and SM, whereas T_{max} (daily maximum LST) correlates with LE and VIs. Regarding other temperature-related parameters, T_0 (LST around sunrise), T_a (temperature rise during daytime), and δT (temperature fall during nighttime) are unstable in quantification by DTC model. Moreover, time-related parameters, such as t_m (time reaching T_{max}), are more sensitive to topographic slope and geometric conditions than surface thermal properties at humid sites in East Asia, although they correlate with EF and SM at a semi-arid site in Australia. Additionally, the spatial distribution of the DTR anomaly during the 2018 heat wave corresponds with the drying signals indicated as negative SM anomalies. Regions with large positive anomalies in T_{max} and DTR correspond to area with visible damage to vegetation, as indicated by negative VI anomalies. Hence, combined T_{max} and DTR potentially detects vegetation drying indetectable by VIs, thereby providing earlier and more detailed vegetation monitoring in both humid and semi-arid climates.

1. Introduction

Land surface temperature (LST) is driven by solar radiation, atmospheric conditions, and surface properties including thermal inertia, albedo, and roughness (Ignatov and Gutman, 1999; Li et al., 2013). LST is also affected by plant transpiration at vegetation canopy surfaces (Pallas et al., 1967; Urban et al., 2017; Konrad et al., 2021). As such LST provides important insights regarding surface energy-, water-, and carbon budgets. Diurnal-scale changes in LST are associated with atmospheric local circulations including sea–land breezes, mountain–valley

breezes, and urban-rural breezes (Saitoh et al., 1996; Yamamoto and Ishikawa, 2020), variations in solar radiation and soil moisture (SM)- (Gillies et al., 1997; Verstraeten et al., 2006), as well as transpiration changes due to midday photosynthesis depression (so-called water stress) and high temperature plant injury (Damm et al., 2010; Liu et al., 2017; Paul-Limoges et al., 2018).

Recent geostationary satellites, such as the Himawari-8, Geostationary Operational Environmental Satellite R-Series (GOES-R), Geostationary Korea Multi-Purpose Satellite-2A (GEO-KOMPSAT-2A), and FengYun-4A, provide diurnal LST changes over a wide area (Xu et al., 2014; Yamamoto et al., 2018; Wang et al., 2019; Zhou and Cheng, 2020). The optical sensors onboard these satellites markedly improved temporal- and spectral resolutions compared with conventional sensors. The derived diurnal-scale LSTs have been successfully applied to estimate a sea breeze cooling effect and land use-dependent thermal inertia in coastal urban areas (Yamamoto and Ishikawa, 2020), as well as for the estimation of diurnal cycles of heat island intensity (Chang et al., 2021). Vegetation monitoring via estimation of evapotranspiration (ET) and gross primary production (GPP) on a diurnal scale is also expected (Fisher et al., 2020; Khan et al., 2021; Xiao et al., 2021). Indeed, diurnal-scale ET and GPP detects plant water stress under hot and arid conditions, potentially contributing to agricultural fields (Green et al., 2022).

Two approaches have been applied to extract and analyze diurnal change characteristics of LST: (1) semi-empirical model (Göttsche and Olesen, 2001; Quan et al., 2014; Weng and Fu, 2014; Sismanidis et al., 2017), and (2) statistical analysis (Ignatov and Gutman, 1999; Aires et al., 2004; Yamamoto and Ishikawa, 2020). A semi-empirical model approach has been applied to the diurnal temperature cycle (DTC) model consisting of functions based on the thermal diffusion equation during daytime, and Newton's law of cooling at nighttime (Göttsche and Olesen, 2009; Duan et al., 2013; Hong et al., 2018). By fitting a DTC model to observed diurnal LSTs, fitting parameters (DTC parameters) can be obtained to characterize the diurnal cycle waveform. Assuming that the diurnal LSTs follow the DTC model function, the diurnal change characteristics can be stably extracted by interpolating the short-time missing data and noise. Indeed, diurnal LSTs with missing data and noise cannot be directly used to accurately represent diurnal change characteristics. Of note, various functions have been developed for the DTC models, each with its own fitting bias (Duan et al., 2012; Chang et al., 2020).

DTC parameters obtained from geostationary satellite-derived LSTs have the potential to provide detailed surface thermal properties related to vegetation drought and health during extreme heat events. However, several issues remain. Practical application of DTC parameters requires quantitative analysis of the relationships with surface thermal properties under realistic conditions, including short-term missing data and noise caused by cloud cover. Especially in humid climate regions, larger uncertainties in DTC parameters and additionally weaker drying signal of vegetation are expected compared to semi-arid regions. Moreover, satellite-derived diurnal LSTs also present biases due to topography. As such, the use of regional-scale DTC parameters requires an understanding of which DTC parameters provide reliable and meaningful data. Previous studies have qualitatively discussed the relationship of DTC parameters to vegetation index (VI) and land cover (Göttsche and Olesen, 2001; Duan et al., 2014). Furthermore, applications of the DTC model have been limited to ideal conditions, e.g., composited LSTs or LSTs measured on a fully clear-sky day (e.g., Inamdar et al., 2008; Duan et al., 2012; Hong et al., 2018).

The current study seeks to addresses these issues by establishing the applicability of DTC parameters obtained from the Himawari-8 LSTs around Japan and the Korean Peninsula. A particular focus is placed on the 2018 heat wave, as a case study, for which the sensitivity of DTC parameters to the vegetation drying signals were investigated. The 2018 heat wave was one of the hottest in the history of the Japan Meteorological Agency (JMA), within the past 60 years (Shimpo et al., 2019). Japan and the Korean Peninsula have a complex terrain and humid climate, resulting in the generation of clouds of various spatiotemporal scales. Hence, comprehensive analysis of the DTC parameters in this region provides a theoretical basis for the application of geostationary satellites for vegetation monitoring. Additionally, the impacts of the East Asia heat wave on terrestrial environments were assessed in this work to gain a better understanding of the associated natural and human systems (Dousset et al., 2011; Lorenz et al., 2013; Jiang et al., 2015; Skinner et al., 2018; Albergel et al., 2019).

2. Data and methods

2.1. Area description

This analysis focused on East Asia covering the Korean Peninsula and the main Japanese islands (Fig. 1). The study area is primarily classified as a humid subtropical climate (Cfa) by Köppen and Geiger, with the hot-summer humid continental climate (Dfa) and the warm-summer humid continental climate (Dfb) distributed in the highlands and the north (Beck et al., 2018). The land cover is primarily composed of dense forests and agricultural croplands (Fig. 1a). The highlands containing forests are distributed on the east side of the Korean Peninsula and the inland Japan (Fig. 1). In contrast, the west side of the Korean Peninsula and the coastal area of Japan have low altitudes, including widely distributed agricultural land and built-up areas.

The heat wave occurred throughout Japan and Korea from mid-July to early August 2018 (Shimpo et al., 2019). The cumulative number of extremely hot days, when the daily maximum surface air temperature exceeded 35 °C, was the highest in the history of JMA observations. A total of 1455 fatalities occurred due to heat stroke from July to August 2018, which was more than twice the average from 2015 to 2021 (Japanese Ministry of Health, Labour and Welfare, 2021).

The primary factors contributing to this heat wave included the extension- and maintenance of the Tibetan High in the upper troposphere, and the North Pacific Subtropical High (NPSH) in the lower troposphere (Fig. 2a and b). The influence of heat waves was enhanced in areas where the positive anomalies of the Tibetan High and NPSH overlapped (Double-High structure) (Shimpo et al., 2019). The Double-High structure caused surface heating via anomalous high solar radiation, and adiabatic heating via anomalous descent. The extension of the Tibetan High and NPSH were attributed to atmospheric teleconnections from meandering of the subtropical jet stream (Enomoto et al., 2003; Kosaka et al., 2009) and enhanced convective activity around the Philippines (Nitta, 1987; Kosaka and Nakamura, 2010), respectively. Moreover, Imada et al. (2019) argued that anthropogenic global warming was likely acting as a background of the 2018 heat wave around Japan, and that the occurrence of such heat waves will increase in the future. In this study, the mean pressure patterns at 200-hPa and 850-hPa over the study period are expressed as deviations from the spatial mean of geopotential heights in the analysis domain (Fig. 2a and b). The stronger heat wave caused by the Double-High area was defined as an area with positive anomalies at 200-hPa and 850-hPa higher than +20 m (corresponds to Tibetan High) and + 10 m (corresponds to NPSH), respectively (Fig. 2c).

2.2. Data

2.2.1. In situ measurements

Relationships between DTC parameters and daily vegetation activities under a humid climate were investigated using up- and downwelling longwave radiation (LR$_u$ and LR$_d$, respectively), downwelling shortwave radiation (SR$_d$), latent heat flux (LE), sensible heat flux (H), and GPP observed, or estimated, at four vegetation sites (Table 1): Takayama deciduous broadleaf forest site (TKY; Saigusa et al., 2005), Cheorwon rice paddy site (CRK; Hwang et al., 2020), Gwangneung coniferous forest site (GCK; Kang et al., 2017), and Gwangneung deciduous forest site (GDK; Kang et al., 2017). These sites are registered in
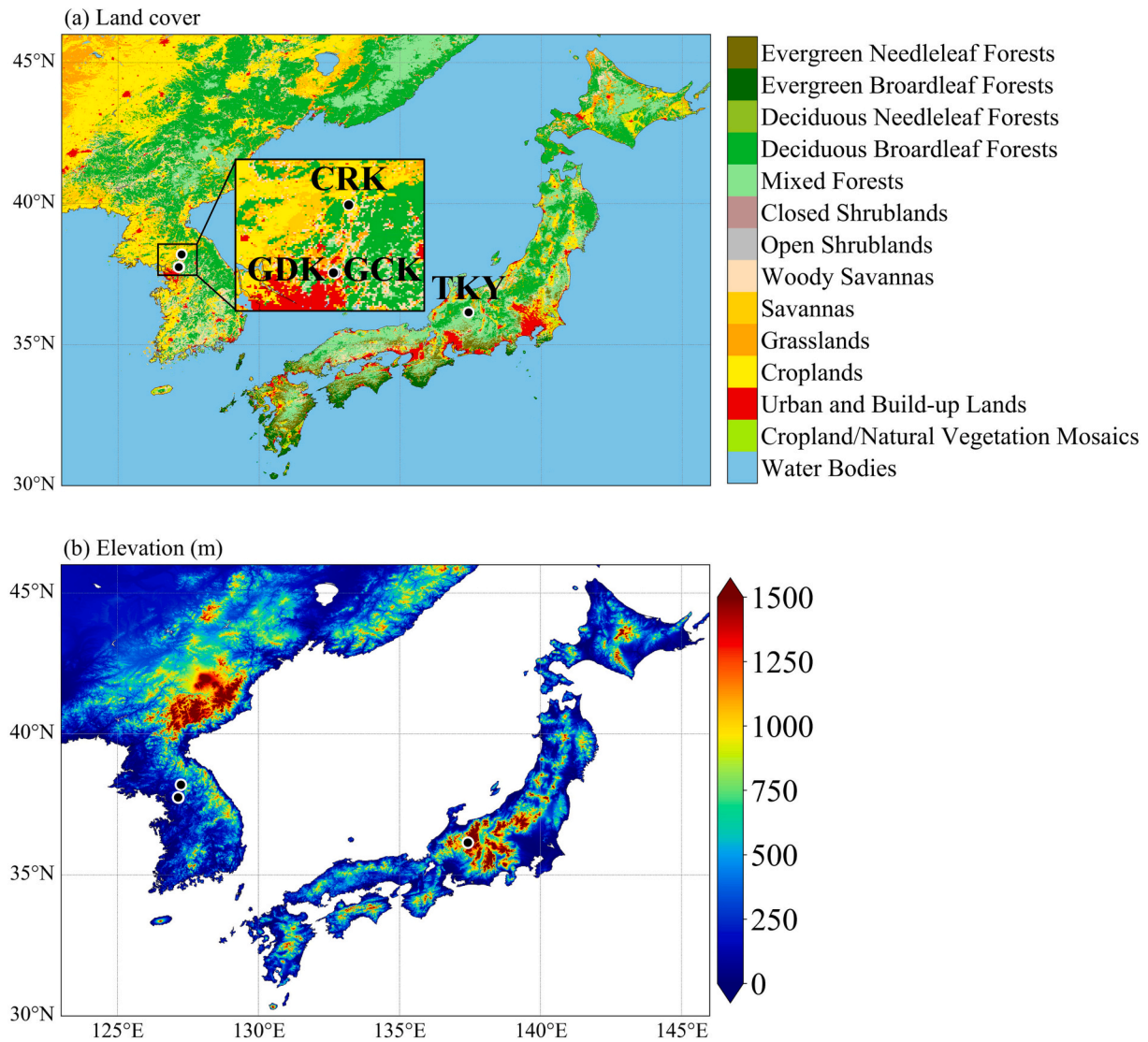
(a) Land cover

(b) Elevation (m)

Fig. 1. Spatial distributions of (a) land cover types (MCD12Q1 Collection 6 product; Sulla-Menashe et al., 2019) and (b) elevation (Shuttle Radar Topography Mission 30 data; Farr and Kobrick, 2000; Farr et al., 2007) in the study area. The distribution of collection sites are also presented; TKY: Takayama deciduous broadleaf forest site, CRK: Cheorwon rice paddy site, GCK: Gwangneung coniferous forest site, GDK: Gwangneung deciduous forest site.

AsiaFlux (https://asiaflux.net/). The location of each site is presented in Fig. 1. Observations were provided every 30 min, and those from July 1 to August 31, 2015 to 2018 were used. Information on the instruments and mounting heights used to collect the observation data are listed in Table 1.

In situ LSTs were estimated using the up- and down-welling long-wave radiation, as denoted in Eq. (1):

$$LST = \left[\frac{LR_u - (1 - \varepsilon_b)LR_d}{\sigma \bullet \varepsilon_b} \right]^{1/4} \qquad (1)$$

where LR_u and LR_d represent the upwelling and downwelling longwave radiation (W·m^{-2}), respectively; σ is the Stefan–Boltzmann constant (5.67×10^{-8} W·m^{-2}·K^{-4}); and ε_b is the surface broadband emissivity. Of note, ε_b at each site was estimated from the ASTER Global Emissivity Database (Hulley et al., 2015) at 100 m resolution using the conversion formula presented in Eq. (2) (Cheng et al., 2013):

$$\varepsilon_b = 0.197 + 0.025\varepsilon_{10} + 0.057\varepsilon_{11} + 0.237\varepsilon_{12} + 0.333\varepsilon_{13} + 0.146\varepsilon_{14} \qquad (2)$$

where ε_{10}–ε_{14} are the land surface emissivities (LSEs) of ASTER bands 10–14, respectively.

In order to investigate the performance of DTC parameters in drying detection under climatic conditions outside of East Asia, data from the Alice Spring Mulga (ASM) and Cumberland Plain (CLP) sites in Australia were used. The ASM site is a woodland located at 133.249°E, 22.283°S and has a semi-arid climate with mean annual precipitation of ~300 mm. CLP site is a woodland located at 150.724°E, 33.615°S, and has a warm temperate climate with mean annual precipitation of ~800 mm. Both sites receive less precipitation than the TKY, CRK, GCK, and GDK sites (mean annual precipitation of about 2300 mm, 1400 mm, 1300 mm, and 1300 mm, respectively). The sites are registered in OzFlux (http://www.ozflux.org.au/), and they provide a dataset (processing level 6) including GPP data. LR$_u$, LR$_d$, LE, H, GPP, and SM were used. Observations were provided every 30 min, and those from January 1 to February 28, 2015 to 2021 were used.

2.2.2. Himawari-8/AHI LST data

Himawari-8 was launched in October 2014 and began observations in July 2015 (Bessho et al., 2016). It flies over the equator at 140.7°E, and the main observation area comprises East Asia and Oceania. The Advanced Himawari Imager (AHI) onboard Himawari-8 contains six visible (VIS) and near infrared (NIR) bands centered at 0.47, 0.51, 0.64,
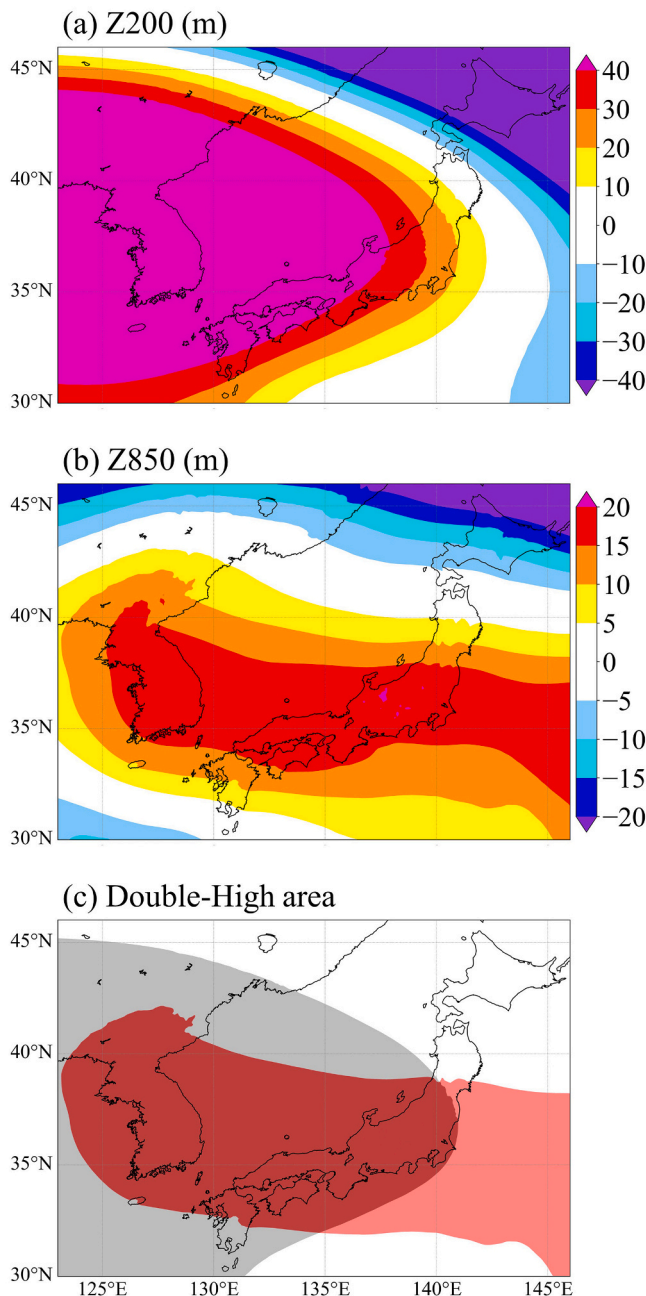
(a) Z200 (m)

(b) Z850 (m)

(c) Double-High area

Fig. 2. Geopotential height anomalies at (a) 200 hPa and (b) 850 hPa averaged from July 16 to August 5, 2018. (c) Double-High area where the mean geopotential height anomalies at 200-hPa and 850-hPa were higher than +20 m (gray) and + 10 m (red), respectively. (For interpretation of the references to colour in this figure legend, the reader is referred to the web version of this article.)

0.86, 1.61, and 2.25 μm, as well as ten infrared (IR) bands centered at 3.9, 6.2, 6.9, 7.3, 8.6, 9.6, 10.4, 11.2, 12.4 and 13.3 μm. The observation cycle is 10 min for the full disk. The spatial resolution of thermal infrared (TIR) bands to retrieve LST are approximately 2 km.

LST was retrieved from Himawari-8 data using a multi-band method developed by Yamamoto et al. (2018). This requires brightness temperatures and LSEs of three AHI TIR bands as the inputs. The Himawari-8 data were distributed by the Center for Environmental Remote Sensing (CEReS), Chiba University, Japan as geometrically corrected and resampled to a geographic coordinate (Takenaka et al., 2020; Yamamoto et al., 2020). The resampled spatial resolutions of thermal IR bands are

0.02° and the temporal resolutions are 10 min. The LSEs in the AHI TIR bands were estimated by a semi-empirical method based on land cover information and normalized difference vegetation index (NDVI) (Yamamoto and Ishikawa, 2018). Cloud screening was conducted using a multispectral threshold method based on one VIS, two NIR, and four IR bands as a preprocessing step of the LST retrieval (Yamamoto et al., 2022). Uncertainty of the LST retrieval is below 1.0 °C for a pixel with small spatial and spectral variability of the LSEs, such as a fully vegetated pixel (Yamamoto et al., 2022).

2.2.3. Auxiliary data

Spatiotemporal characteristics of the DTC parameters from Himawari-8 LSTs were investigated by comparison with satellite and numerical model products related to vegetation activity and moisture content (Table 2).

The Terra and Aqua Moderate Resolution Imaging Spectroradiometer (MODIS) International Geosphere Biosphere Programme (IGBP) land cover data from the MCD12Q1 Collection 6 product (Sulla-Menashe et al., 2019; Fig. 1a) were used to investigate the DTC parameters for different types of land cover. The land cover data with the most frequent class for each pixel in 2015–2019 was used. IGBP land cover was classified into three types: vegetation (classes 1–5), cropland (classes 12 and 14), and urban (class 13). Other classes were not considered in this analysis due to their small coverage.

The Suomi National Polar-Orbiting Partnership (S-NPP) NASA Visible Infrared Imaging Radiometer Suite (VIIRS) enhanced vegetation index (EVI) and NDVI data (VNP13A1; Didan and Barreto, 2018) were used to investigate the spatiotemporal variabilities of vegetation. Products were generated as 8-day composites, and data for the 24 days from July 13 to August 5 (three 8-day periods) in 2015–2021 were applied for analyses. The spatial resolution was approximately 500 m, and was resampled using bilinear interpolation of the 0.02° grid when directly compared with the DTC model parameters.

The LE and potential LE (PLE) data from MOD16A2 Version 6 (Mu et al., 2011) were used to assess the spatiotemporal variability of the surface moisture conditions. The PLE data was used to calculate the LE to PLE ratio (LE/PLE) as an indicator of surface wetness (Yuan et al., 2007). The datasets were estimated based on the Penman-Monteith equation using land cover, fraction of absorbed photosynthetically active radiation/leaf area index, and albedo from the MODIS products, as well as the meteorological data from the Modern-Era Retrospective Analysis for Research and Applications produced by the NASA's Global Modeling and Assimilation Office. Data processing methods were the same as those applied for the VIIRS EVI and the NDVI data as the composite number of days and spatial resolution of the product are the same as for VNP13A1.

The surface SM data of the Soil Moisture Active Passive (SMAP) global SM dataset (Mladenova et al., 2019, 2020) was used to analyze the spatiotemporal variability of SM content at the land surface. This dataset was generated by assimilating satellite-derived SMAP Level-3 SM observations into the modified two-layer Palmer model using a one-dimensional Ensemble Kalman Filter data assimilation method (Mladenova et al., 2020). The data were generated 3 days apart, and the 21-day period from July 16 to August 5 in 2015–2021 was incorporated into the analysis. The spatial resolution was 10 km.

Geopotential height data at 200-hPa and 850-hPa from July 16 to August 5, 2018 were used to extract the area for the Double-High structure (Fig. 2). These data were the initial values employed in the prediction of the meso-scale model of the Japan Meteorological Agency (JMA-MSM; Saito et al., 2006) which is a numerical weather prediction model. The spatial resolution is 0.1° in the north-south direction and 0.125° in the east-west direction, while the temporal resolution is 3 h (00, 03, 06, 09, 12, 15, 18, and 21 coordinated universal time (UTC)).

Table 1

Site information used in this study.

Site name	Takayama deciduous broadleaf forest	Cheorwon rice paddy	Gwangreung coniferous forest	Gwangreung deciduous forest
Site code	TKY	CRK	GCK	GDK
Location	36.146°N	38.201°N	37.748°N	37.749°N
	137.423°E	127.251°E	127.162°E	127.149°E
Altitude	1420 m	181 m	132 m	252 m
Vegetation type	Cool temperate deciduous forest	Rice paddy	Coniferous forest	Mixed deciduous forest
Canopy height	15–20 m	~1 m	28 m	20 m
Sensor (SR$_d$, LR$_u$, LR$_d$)	MR-50,	CNR4,	CNR1,	CNR1,
	EKO Co., Japan	Kipp & Zonen B.V., Netherlands	Kipp & Zonen B.V., Netherlands	Kipp & Zonen B.V., Netherlands
Sensor (CO$_2$, LE, H)				
- 3D sonic anemometer	DA600-3TV,	CSAT3, Campbell Sci., Inc., USA	CSAT3, Campbell Sci., Inc., USA	CSAT3, Campbell Sci., Inc., USA
	KAIJO Co., Japan			
- Infrared gas analyzer	LI-6262,	LI-7200,	LI-7200,	EC155, Campbell Sci., Inc., USA
	LI-COR Inc., USA	LI-COR Inc., USA	LI-COR Inc., USA	
Mounting height	25 m	10 m	40 m	38 m
Reference	Saigusa et al. (2005)	Hwang et al. (2020)	Kang et al. (2017)	Kang et al. (2017)

Table 2

Summary of satellite and numerical model products.

Product	Unit	Spatial Resolution	Temporal Resolution	Product Short name	Reference
Land surface temperature (LST)	°C	0.2°	10-min	AHI LST	Yamamoto et al. (2022)
Normalized difference vegetation index (NDVI)		500 m	8-day	VNP13A1	Didan and Barreto (2018)
Enhanced vegetation index (EVI)					
Latent heat flux (LE)	W·m^{-2}	500 m	8-day	MOD16A2	Mu et al. (2011)
Potential LE (PLE)					
Surface soil moisture (SM)	mm	10 km	3-day	SMAP	Mladenova et al. (2019)
Land cover classification		500 m	1-year	MCD12Q1	Sulla-Menashe et al. (2019)
Geopotential heights at 200-hPa and 850-hPa	m	0.1° × 0.125°	3-h	JMA-MSM	Saito et al. (2006)

2.3. Methods

2.3.1. Diurnal temperature cycle model

The DTC model proposed by Inamdar et al. (2008), which has stable fitting accuracy compared with several different DTC models (Duan et al., 2012), was applied. The LST change at daytime (T_d) was modeled by a cosine function based on the thermal diffusion equation, and the LST decay at nighttime (T_n) was described by a hyperbolic function (Fig. 3). The T_d and T_n are expressed according to Eqs. (3)–(6):

$$T_d(t) = T_0 + T_a cos\left(\frac{\pi}{\omega}(t - t_m)\right), t < t_s \tag{3}$$

$$T_n(t) = T_0 + \delta T + \left[T_a cos\left(\frac{\pi}{\omega}(t_s - t_m)\right) - \delta T\right]\frac{k}{(k + t - t_s)}, t \geq t_s \tag{4}$$

with

$$\omega = \frac{4}{3}(t_m - t_{sr}) \tag{5}$$

$$k = \frac{\omega}{\pi}\left[cot\left(\frac{\pi}{\omega}(t_s - t_m)\right) - \frac{\delta T}{T_a}cosec\left(\frac{\pi}{\omega}(t_s - t_m)\right)\right] \tag{6}$$

where t represents the time; T_0 is the residual temperature around sunrise (°C); T_a is the temperature amplitude (°C); ω is the half-period of the cosine term (h); t_m is the time of the daily maximum temperature (solar time); t_s is the start time of the attenuation function $T_n(t)$ (solar time); δT is the temperature difference between T_0 and $T_n(t \to \infty)$ (°C); $T_n(t \to \infty)$ represents the temperature when LST reaches equilibrium with the near-surface air temperature, and δT is calculated as $T_n(t \to \infty) - T_0$; k is the attenuation constant (h); and t_{sr} is the sunrise time (solar time) (Fig. 3).

The T_0, T_a, δT, t_m, and t_s model parameters were estimated as fitting parameters (DTC parameters) based on Eqs. (3) and (4) using the diurnal LST change retrieved from Himawari-8 data. Additionally, ω and k were calculated from Eqs. (5) and (6), respectively (Duan et al., 2013).
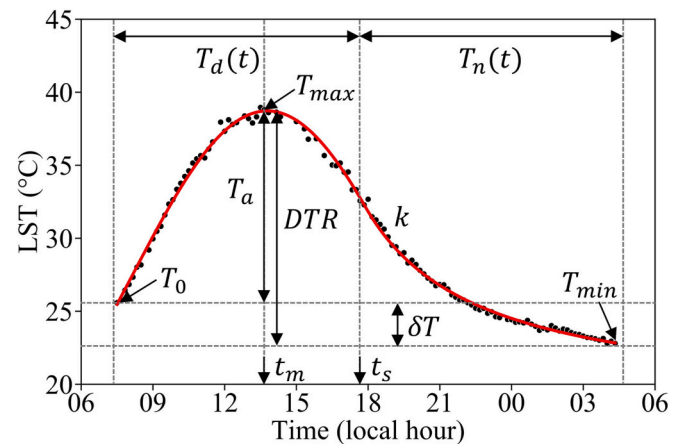
Fig. 3. Fitting of the diurnal temperature cycle (DTC) model (red line) to diurnal variations in land surface temperatures (LSTs; dot) of a pixel on a clear-sky day. $T_d(t)$ and $T_n(t)$ are daytime and nighttime LSTs, respectively, expressed as a function of time (hour). T_0 is the residual temperature around sunrise; T_a is the temperature amplitude; t_m is the time of the daily maximum temperature (solar time); t_s is the start time of the attenuation function $T_n(t)$ (solar time); δT is the temperature difference between T_0 and T ($t \to \infty$) (°C); T_{max} is the maximum daily temperature ($T_{max} = T_0 + T_a$); T_{min} is the minimum daily temperature ($T_{min} = T_0 + \delta T$); DTR is the diurnal temperature range ($DTR = T_a - \delta T$); k is the attenuation constant (hour). The Himawari-8 LSTs were estimated on 21 July 2018 at a pixel corresponding to 37.76°N, 127.12°E. (For interpretation of the references to colour in this figure legend, the reader is referred to the web version of this article.)

Meanwhile, t_{sr} is calculated from solar geometry as the local solar time in each pixel. The fitting was applied using LSTs from 2 h after sunrise to 1 h before sunrise on the following day to avoid the weakness of the model during the sunrise/sunset hours (Duan et al., 2014). Diurnal

temperature cycle parameters were used for the sunny day when the root mean square error (RMSE) of fitting was <0.5 °C for each pixel. Cases where fitting was judged to have not converged ($\delta T \leq -20$, $t_m \leq 10.5$ or $t_m \geq 15$, $t_s \leq 15$ or $t_s \geq 19$) were excluded from analysis. Most cases with large data gaps did not converge in the fitting and hence were excluded.

The advantage of applying the DTC model is not only to facilitate quantification of diurnal properties, but also for cloud screening. That is, assuming that the observed diurnal LSTs follow a function of the DTC model, the DTC parameters can be obtained by removing outliers and interpolating short-term missing values. Direct extraction of diurnal characteristics from observed diurnal LSTs is sensitive to outliers and missing values. Moreover, a distorted diurnal change wave, containing cooled LSTs after long-term cloud cover or cloud-mixed LSTs due to misjudgment of clear-skies, cannot be readily applied for drying detection as it can lead to false detection. Such cases can be systematically excluded from the analysis as fitting failures of the DTC model.

2.3.2. Analysis of DTC parameters obtained from in situ LST

Before examining DTC parameters obtained from the Himawari-8 LSTs, we examined DTC parameters obtained from in situ LSTs free from missing data due to cloud cover or bias caused by satellite viewing geometry. The DTC parameters were obtained from in situ LSTs estimated every 30 min, and they were used for analysis during days when the daily integrated downward shortwave radiation was >15 MJ·m^{-2}·day^{-1} and fitting of the DTC model converged. The considered DTC parameters included daily maximum temperature ($T_{max} = T_0 + T_a$), daily minimum temperature ($T_{min} = T_0 + \delta T$), diurnal temperature range ($DTR = T_a - \delta T$), k (Eq. (6)), T_0, T_a, δT, t_m, and t_s (Fig. 3).

Obtained in situ DTC parameters were compared with daily LE, evaporative fraction (EF = LE/(H + LE)), and GPP during July–August 2015–2018. These comparisons were made to assess the relationships between DTC parameters and evapotranspiration or photosynthesis over vegetated surfaces in a humid climate. The daily EF was used as an indicator of the soil or vegetation moisture conditions (Yuan et al., 2007). A decrease in EF indicates a decrease in the partitioning of radiant energy to the surface into the latent heat flux, suggesting a stronger moisture limitation. The EF does not always depend on the moisture conditions of the soil or vegetation surface, because latent heat fluxes also depend on atmospheric demand.

Similar analyses were performed for the ASM and CLP sites in Australia. These sites receive less precipitation than East Asia, thus clearer responses of LST and vegetation activity to hotter/drier conditions can be expected. The study period includes extreme events such as the 2019 heat wave (Qiu et al., 2020). By comparing the results with those for East Asia, we discuss the differences in the performance of the DTC parameters in drying detection depending on the climatic conditions. The results are described in the Discussion section.

2.3.3. Analysis of DTC parameters obtained from Himawari-8 LST

The spatial distribution characteristics of DTC parameters obtained from the Himawari-8 LSTs were investigated. The DTC parameters for the study area were estimated from July 16 to August 5, 2015–2021. This 21-day period was set based on the duration of anticyclonic anomalies behind this heat wave (Shimpo et al., 2019). The means of the DTC parameters for 2018 represented the heat wave, whereas those from 2015 to 2021, excluding 2018, were used as reference values.

The spatial distributions of reference DTC parameters were compared with those of environmental factors (NDVI, EVI, LE, LE/PLE, and SM). For the 2018 heat wave, the anomalies in DTC parameters (deviations from the reference values) were compared with those of environmental factors, with a focus on the Double-High area (Fig. 2c). In addition to spatial analyses, temporal correlations between DTC parameters and SM were also examined by comparing changes every 3 days throughout the analysis period. These analyses provided insights regarding the relationship between DTC parameters and surface thermal

properties, as well as their applicability to the detection of heating and drying. Moreover, we discussed the impact of the heat wave on terrestrial vegetation.

3. Results

3.1. Validity of DTC parameters obtained from fitting

T_{max}, T_{min}, DTR, t_m, and t_s were obtained stably in the fitting of the DTC model, whereas the solutions for T_0, T_a, δT, and k were unstable. A discrepancy was observed in the T_0 obtained from the in situ LSTs compared with the observations, whereas those for T_{max} and t_m were in agreement (Fig. 4). More specifically, the T_0 corresponded to LST around 8:00 to 9:00 a.m., rather than LST at the earliest time. The discrepancy was due to the calculation method for ω (Eq. 5), which followed the method proposed by Duan et al. (2013). If the fittings were performed with the ω calculation as $5/3(t_m - t_{sr})$ instead of $4/3(t_m - t_{sr})$, T_0 became closer to the earlier morning LSTs (Fig. S1). T_a and δT also varied with decreasing T_0, maintaining unchanged T_{max}, T_{min}, DTR, t_m, and t_s.

3.2. Relationship between in situ DTC parameters and daily LE and GPP

Small and large daily LE cases consistently exhibited different diurnal changes in LST at all four sites (Fig. 4a–d). Days with a larger LE had higher T_0, T_a, T_{max}, and DTR; for example, T_0, T_a, T_{max}, and DTR at the CRK site changed by +2.6, +2.6, +5.2, and +8.1 °C respectively (Fig. 4b). However, different trends were observed in δT and T_{min} at each site; for example, T_{min} changed by −2.9 °C at the CRK site and + 4.0 °C at GDK site (Fig. 4b and d). Time-related parameters (t_m, t_s, and k) also changed in different ways in each case; for example, t_m changed by +0.3 h at the TKY site and − 0.6 h at the GCK site (Fig. 4a and c). The changes in T_{max}, T_{min}, DTR, t_m, and t_s corresponding to changes in daily LE were robust to different ω widths (Figs. 4 and S1).

The temperature-related parameters (T_0 T_a, δT, T_{max}, T_{min}, and DTR) were more strongly correlated with daily LE than the time-related parameters (t_m, t_s, and k) (Table 3). In particular, T_a, T_{max}, and DTR were significantly correlated with LE in most cases ($P < 0.01$); for example, T_{max} had correlation coefficients of 0.71, 0.27, 0.31, and 0.38 at the TKY, CRK, GCK, and GDK sites, respectively. T_a and DTR were significantly and negatively correlated with daily EF at the CRK-, GCK-, and GDK sites ($P < 0.05$), however, were positively correlated with daily LE at the same sites. These sites tended to be drier with greater daily LE as the partitioning of energy to H was greater. In contrast, at the TKY site, T_a and DTR were positively correlated with daily EF.

Although the correlations between temperature-related parameters and daily GPP were weak, at all study sites, T_a, δT, and DTR consistently exhibited the same correlation directions (i.e., negative, positive, and negative, respectively). Moreover, focusing on the relationship between DTR and daily GPP (Fig. 5a, c, e, and g), the cases with particularly large DTR had relatively small daily GPP (excluding the GDK site). Additionally, these relatively small daily GPP cases had diurnal variations that differed from those of the mean (Fig. 5b, d, and f). During midday, the diurnal variations tended to be smaller despite higher SR$_d$.

3.3. Spatial variability characteristics of reference DTC parameters

Spatial distributions of the reference T_0, T_a, δT, T_{max}, T_{min}, and DTR values (Fig. 6) corresponded to environmental factors, such as VIs, LE, LE/PLE, and SM (Fig. S2). T_{max} had the highest correlation with NDVI, EVI, LE, and LE/PLE, whereas DTR had the highest correlation with SM (Fig. 7). T_0, T_a, and T_{max} (Fig. 6a and d) showed spatial distribution characteristics that were lower with higher VIs (Fig. S2a and S2b), or higher LE (Fig. S2c and S2d). Related to these, T_0, T_a, and T_{max} negatively correlated with NDVI (−0.54, −0.45, and − 0.69, respectively), EVI (−0.43, −0.38, and − 0.55, respectively), LE (−0.27, −0.44, and − 0.49, respectively), and LE/PLE (−0.32, −0.43, − 0.52,
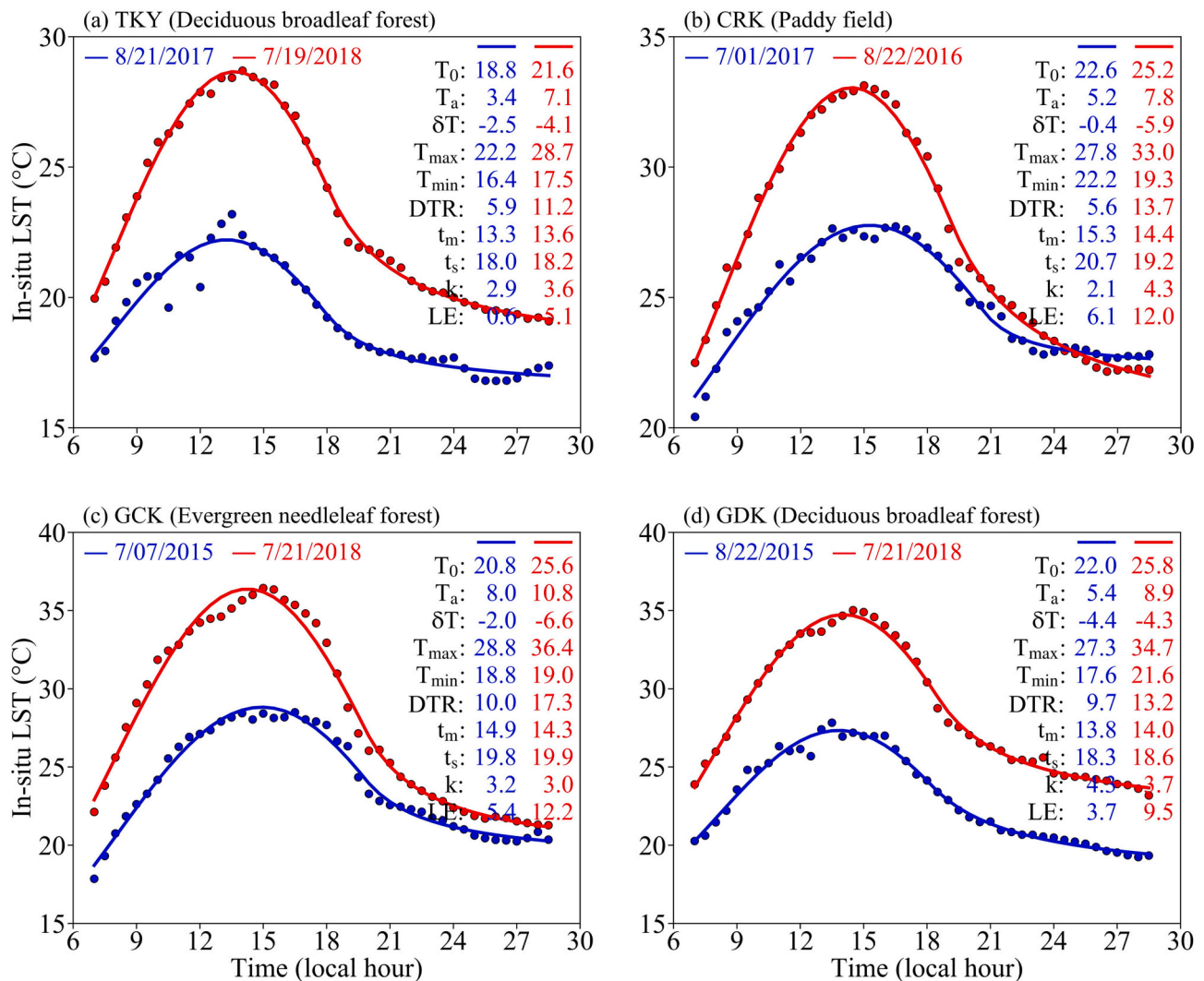
Fig. 4. Diurnal variation in in situ- (dotted) and fitted (solid line) LST with different magnitudes of LE at four sites: (a) TKY, (b) CRK, (c) GCK, and (d) GDK, with estimated DTC parameters. The days with high- (red) and low (blue) LE were selected during July–August 2015–2018. (For interpretation of the references to colour in this figure legend, the reader is referred to the web version of this article.)

Table 3

Correlation coefficients between DTC parameters and daily LE, EF, and GPP observed at flux site observations during July–August 2015–2018.

	Site	T_0	T_a	δT	T_{max}	T_{min}	DTR	t_m	t_s	k
LE	TKY	0.53**	0.47**	−0.32**	0.71**	0.44**	0.57**	0.15	−0.01	0.12
	CRK	0.03	0.36**	−0.40**	0.27**	−0.26**	0.51**	−0.23*	−0.11	0.17
	GCK	0.19	0.27*	−0.24*	0.31**	−0.05	0.33**	−0.11	0.10	−0.03
	GDK	0.28**	0.27**	−0.06	0.38**	0.19	0.17	−0.14	−0.08	−0.03
EF	TKY	0.61**	0.20	−0.41**	0.64**	0.48**	0.44**	0.12	0.01	0.26
	CRK	0.19	−0.30**	0.02	0.02	0.15	−0.20*	−0.17	−0.05	0.03
	GCK	0.09	−0.45**	0.12	−0.12	0.17	−0.30**	−0.14	0.06	−0.11
	GDK	0.03	−0.29**	0.15	−0.08	0.13	−0.25*	0.16	0.10	−0.04
GPP	TKY	−0.25*	−0.06	0.20	−0.25*	−0.16	−0.20	0.21	0.22	−0.12
	CRK	0.40**	−0.20*	0.14	0.38**	0.39**	−0.22*	0.29**	0.22*	0.04
	GCK	−0.27*	−0.43**	0.34**	−0.47**	0.06	−0.49**	0.27*	0.18	−0.14
	GDK	0.17	−0.18	0.02	0.10	0.15	−0.09	0.11	0.39**	−0.17

Significance of correlation are indicated by superscript ** for $P < 0.01$ and * for $0.01 \leq P < 0.05$.

respectively; Fig. 7). Additionally, the δT exhibited correlation coefficients <0.2, as did the T_{min} and DTR calculated using δT relative to those of T_0, T_a, and T_{max}.

T_a and DTR were generally smaller and δT and T_{min} were larger in coastal areas compared with inland areas. T_a, δT, and DTR also exhibited smaller temperature changes in the inland areas of Japan corresponding

to high SM content (Fig. 6b, c, f, and S2e). Related to these, T_a and DTR were negatively correlated with SM (−0.47 and − 0.51, respectively), while δT was positively correlated with SM (0.40) (Fig. 7). T_{max} and T_{min} had relatively small correlation coefficients (−0.32 and 0.22, respectively).

Spatial distributions of the time-related parameters, t_m, t_s, and k
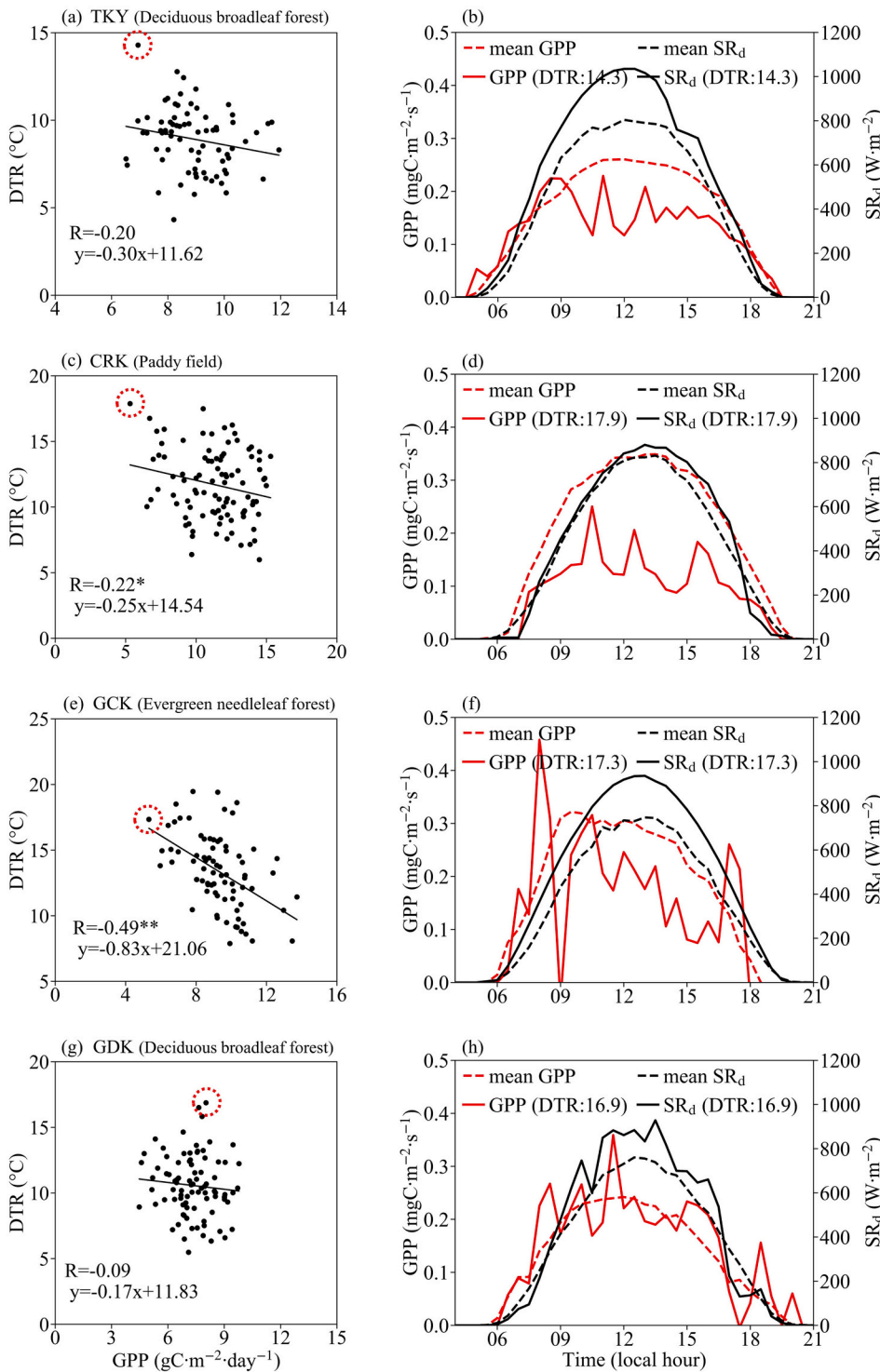
Fig. 5. Relationship between DTR and daily GPP observed at the four flux sites: (a, b) TKY, (c, d) CRK, (e, f) GCK, (g, h) GDK. Left panels show the scatter plots of DTR vs. daily GPP at the four flux sites. Regression analysis results are the same as shown in Table 1, using July–August 2015–2018 observations. ** depicts significant correlation with $P < 0.01$. Right panels show the diurnal changes in GPP (red) and SR_d (black) for the large DTR cases (dashed circles in the left scatter plots). The dashed lines show the mean diurnal change in GPP and SR_d for all the cases shown in the scatter plots in the left. (For interpretation of the references to colour in this figure legend, the reader is referred to the web version of this article.)

(Fig. 6g–i), corresponded to the terrain slope direction (Fig. 1b). t_m, which corresponds to the duration of heating by the sunlight, tended to occur earlier in the north and east sides of terrain and later in the south and west sides. Comparably, t_s and k exhibited similar spatial variability, however, with less clarity than that of t_m. All time-related parameters tended to be larger (later) at higher latitudes, consistent with the notion that higher latitudes have longer daylight hours. Meanwhile, t_m and t_s were weakly and negatively correlated with SM (−0.31 and −0.23, respectively; Fig. 7); t_m, t_s, and k had correlation coefficients <0.20 with all other environmental factors.

3.4. Anomalies in DTC parameters during the heatwave

During the 2018 heat wave, T_{max} and DTR exhibited positive anomalies, and T_{min} had negative anomalies, from the reference values (Fig. 8a–c), roughly corresponding to the Double-High area (Fig. 2c). More specifically, T_{max} showed greater positive anomalies around the Korean Peninsula, where upper-tropospheric anticyclonic anomalies were larger. Meanwhile, the DTR anomalies were larger than those of T_{max} overall, showing areas of above +4 °C in Japan and the Korean Peninsula. The T_{min} anomaly showed a similar spatial distribution to that
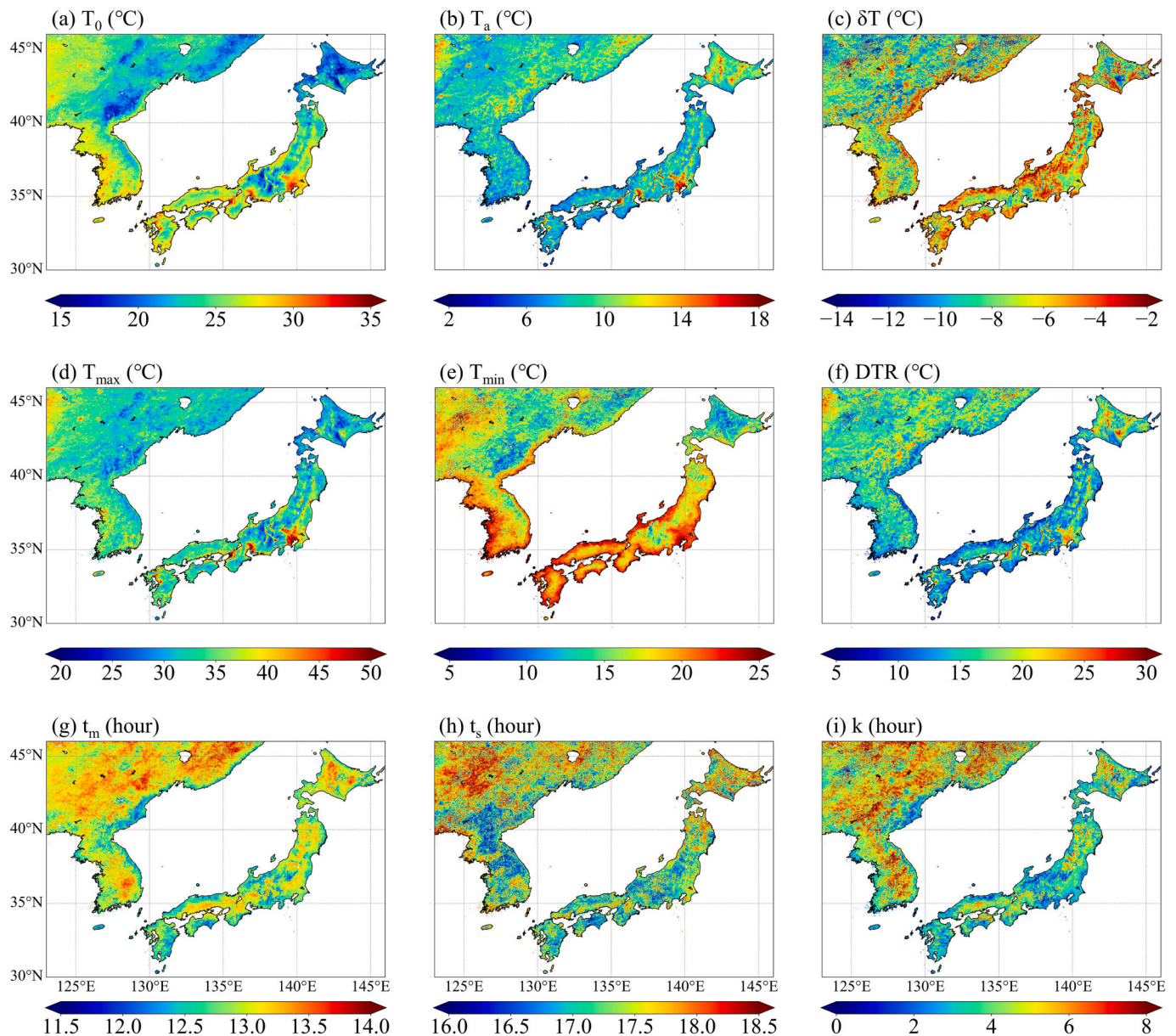
Fig. 6. Spatial distribution of reference DTC parameters: (a) T_0, (b) T_a, (c) δT, (d) T_{max}, (e) T_{min}, (f) DTR, (g) t_m, (h) t_s, and (i) k. The reference values represent the means of those obtained on clear-sky days from July 16 to August 52,015–2021 (excluding 2018).

of *DTR* with the opposite direction. Negative anomalies in SM (indicating drying) corresponded to the Double-High area (Fig. 8f), while negative anomalies in LE/PLE corresponded weakly (Fig. 8e). Negative anomalies in EVI (indicating a decrease in vegetation activity) were clearly distributed around the Korean Peninsula, but not in Japan (Fig. 8d). In contrast, the NDVI anomaly was overall positive in Japan and the Korean Peninsula (Fig. S3d).

The spatial distributions of the T_{min} and *DTR* anomalies overall corresponded to the SM anomaly (Fig. 8), with correlation coefficients of 0.30 and − 0.29, respectively (Fig. S4). Moreover, the LE/PLE anomaly showed drying signals in regions where the T_{min}, *DTR* and SM anomalies were commonly noticeable, such as in the western part of the Korean Peninsula and central Japan. The LE/PLE anomaly, however, exhibited low correlation coefficients with T_{min} and *DTR* anomalies of 0.19 and − 0.16, respectively (Fig. S4). The T_{max} anomaly corresponded to the EVI anomaly in that it was larger around the Korean Peninsula than in Japan. However, their overall spatial distribution did not correspond well, with a low correlation coefficient (−0.14; Fig. S4). Certain areas in

Japan showed positive anomalies in EVI (increased vegetation activity) against positive anomalies in *DTR* and negative anomalies in SM.

The T_{max} anomaly was dominated by the T_0 anomaly rather than the T_a anomaly (Fig. S3a and S3b). Likewise, the T_{min} and *DTR* anomalies were dominated by the δT anomaly rather than the T_0 and T_a anomalies, respectively (Fig. S3a–c). The δT anomaly corresponded to the spatial distribution of SM anomaly, with a correlation coefficient of 0.25 (Fig. S4). T_0 and T_a anomalies had smaller correlation coefficients (0.14 and −0.16, respectively; Fig. S4). The time-related parameter (t_m, t_s, and k) anomalies were not correlated with those of any environmental variables (Fig. S4).

Temporal correlation analysis revealed that T_{max} and *DTR* were significantly and negatively correlated with SM throughout the entire study area (Fig. 9a and c). These results were consistent with those of the spatial correlation analysis (Fig. 7) and corresponds with the SM anomalies observed during the heat wave (Fig. 8). In contrast, T_{min} (Fig. 9b), t_m, and t_s (Fig. S5) did not exhibit consistent correlation across the study area. EVI exhibited a weaker correlation with SM than that of
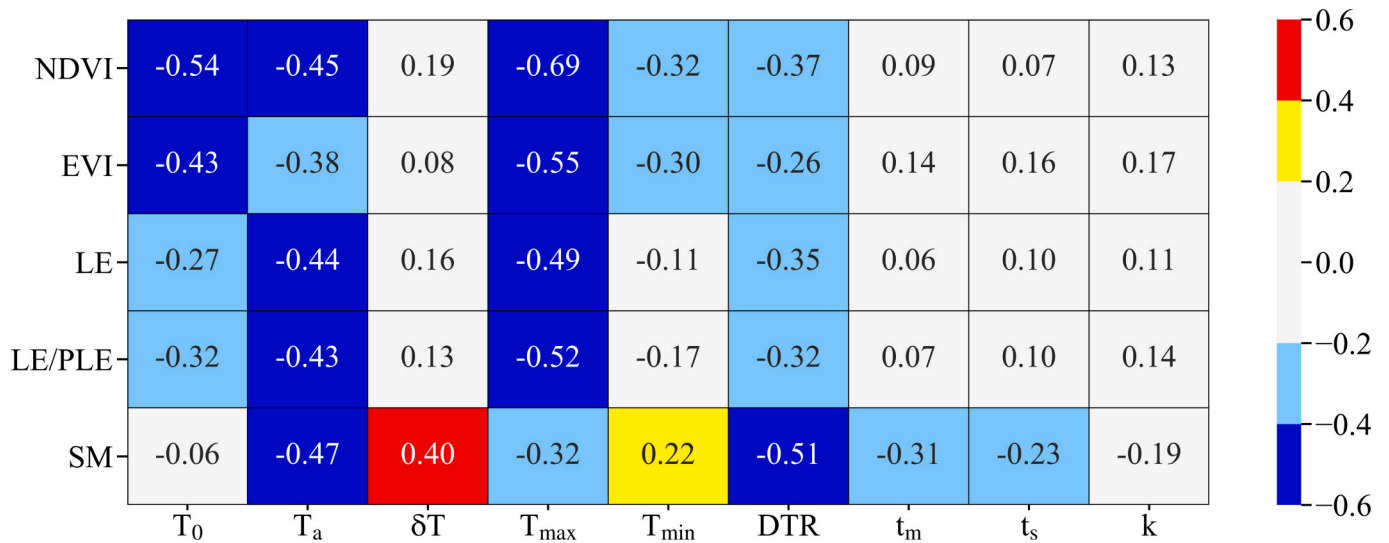
Fig. 7. Correlation coefficients between reference values of DTC parameters and NDVI, EVI, LE, LE/PLE, and SM for the entire study region. The horizontal axis represents DTC parameters; the vertical axis presents environmental factors.
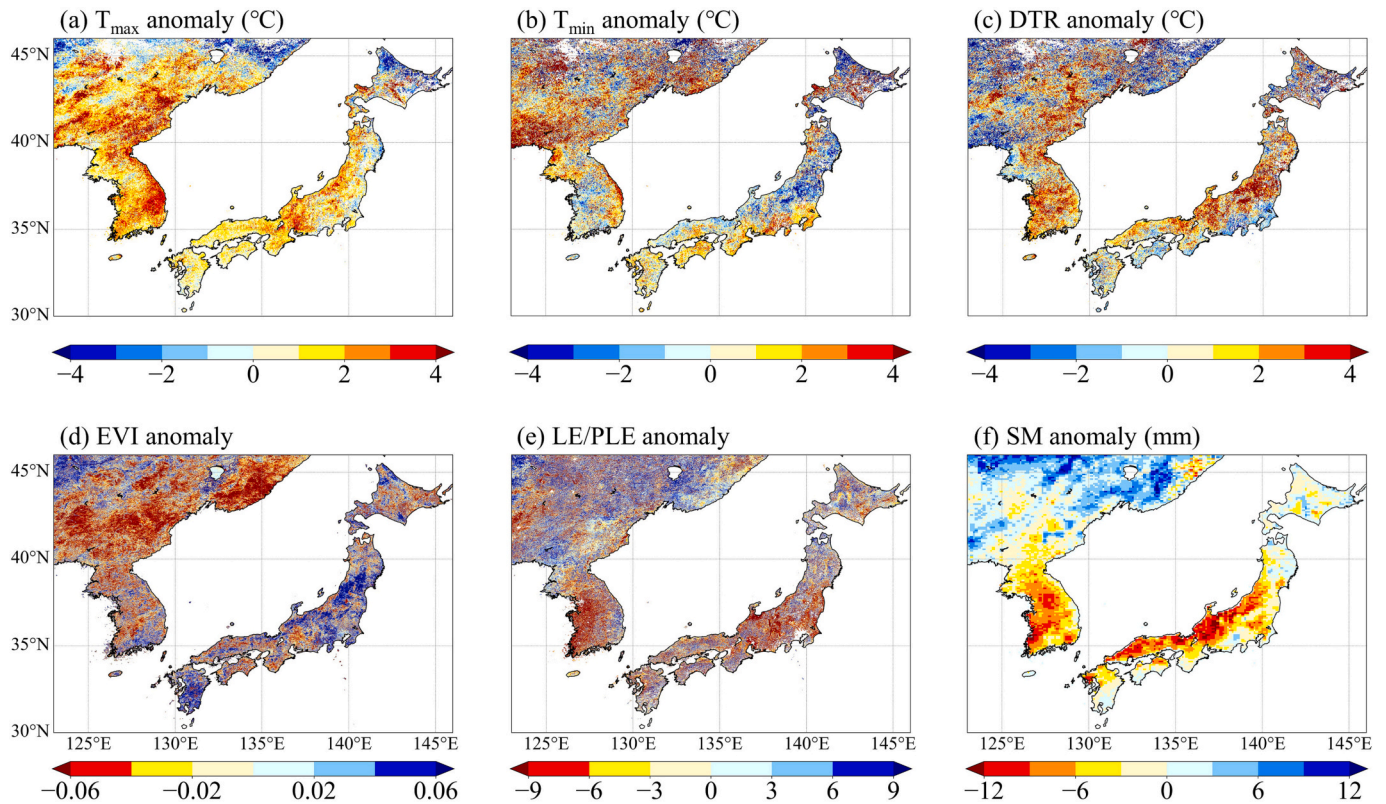

Fig. 8. Spatial distribution of anomalies in (a) T_{max}, (b) T_{min}, (c) DTR, (d) EVI, (e) LE/PLE, and (f) SM from the reference values during the 2018 heat wave (July 16 to August 5, 2018).

temperature-related parameters, and had fewer significant pixels (Fig. 9d). Focusing on a single region where SM decreased largely during the 2018 heat wave, temporal changes in T_{max} and DTR were found to correspond to temporal changes in SM (Fig. S6), consistent with the spatial and temporal correlation results (Figs. 7 and 9). In contrast, T_{min}, t_m, t_s, and EVI did not exhibit temporal changes corresponding to those of SM (Fig. S6).

The anomalies in T_{max} and DTR during the heat wave shown in Fig. 8 were slightly larger in forests and croplands than in urban areas

(Fig. 10a). Distributions of the mean T_{max} and DTR anomalies showed a median of 1–2 °C and reached 5 °C in some forests and croplands. The mean T_{max} anomaly was >0 °C in most cases, whereas the mean DTR anomaly was <0 °C in >25 percentiles of all land cover cases. The distribution of the mean DTR anomaly in urban areas had a median value of ~0. Thus, some cases exhibited an increase in T_{max} with no corresponding increase in DTR; this was especially common in urban areas.

The anomaly distributions for the maximum T_{max} composite (the hottest case for each pixel during the heat wave period; Fig. 10b) were
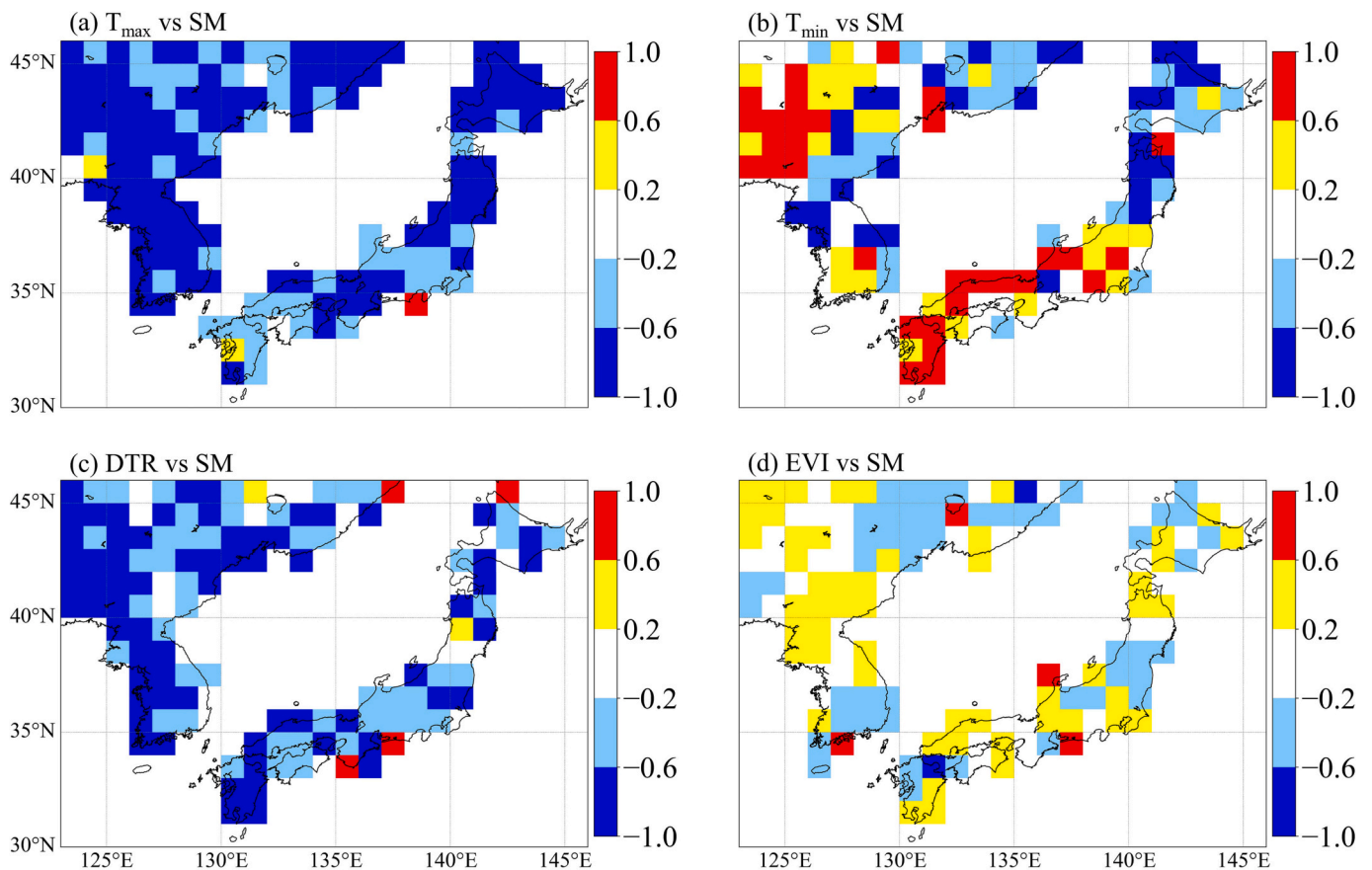
Fig. 9. Spatial distribution of Spearman's rank correlation coefficients between temporal changes in (a) T_{max}, (b) T_{min}, (c) DTR, and SM every 3 days. (d) Spatial distribution of correlation coefficients between temporal changes in EVI and SM every 8 days. Correlation coefficients were averaged over every 1° latitude-longitude grid using cases with $P < 0.05$. Comparisons were made on clear-sky days from July 16 to August 5 in 2015–2021.
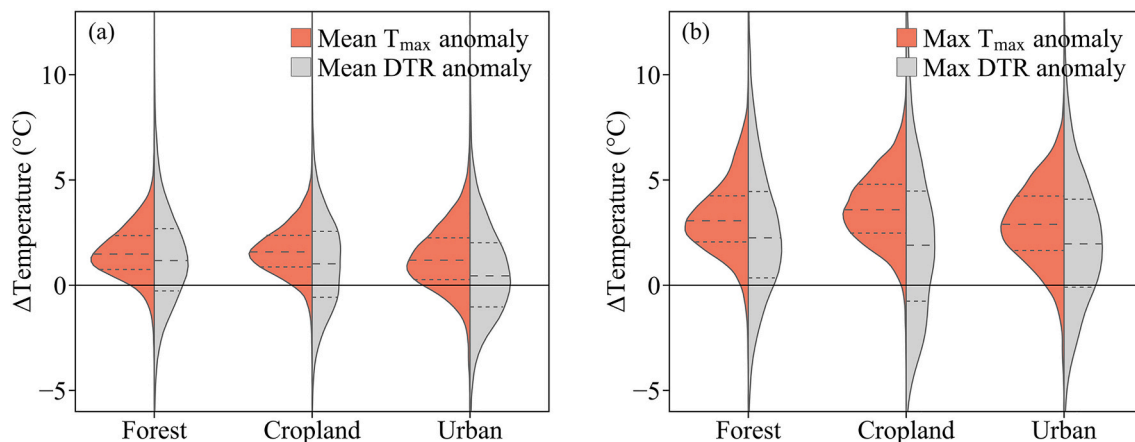

Fig. 10. Probability density distributions of T_{max} (red) and DTR (gray) deviations during the heat wave from the reference values in the Double-High area. Deviations of the (a) mean composites and (b) maximum composites on the day with maximum T_{max} compared with the reference values during the heat wave. IGBP land cover classes 1–5, 12 and 14, and 13 represent forest, cropland, and urban areas, respectively. Dashed lines are medians, and dotted lines are the first and third quartiles. (For interpretation of the references to colour in this figure legend, the reader is referred to the web version of this article.)

positively shifted for T_{max} (approximately +2 °C) and broadened for DTR compared to those for the mean composite (Fig. 10a). Meanwhile, the median for the DTR anomaly did not vary significantly, except in urban areas, with some cases reaching above +10 °C. The positive shifts in the anomaly distributions of T_{max} and DTR in urban areas were greater than those in forests and croplands, and their medians were approximately the same magnitude as those in forests and croplands.

The diurnal change characteristics of LST differed between regions where EVI decreased and did not decrease in response to hotter/drier conditions (Fig. 11). In the region where EVI decreased (Fig. 11a), LST was consistently higher than the reference value throughout the day during the heat wave. The deviations of T_{max} and DTR from the reference values were + 2.5 °C and + 2.8 °C, respectively, while T_{min} exhibited the smallest variation of −0.3 °C. Meanwhile, in the region where EVI did
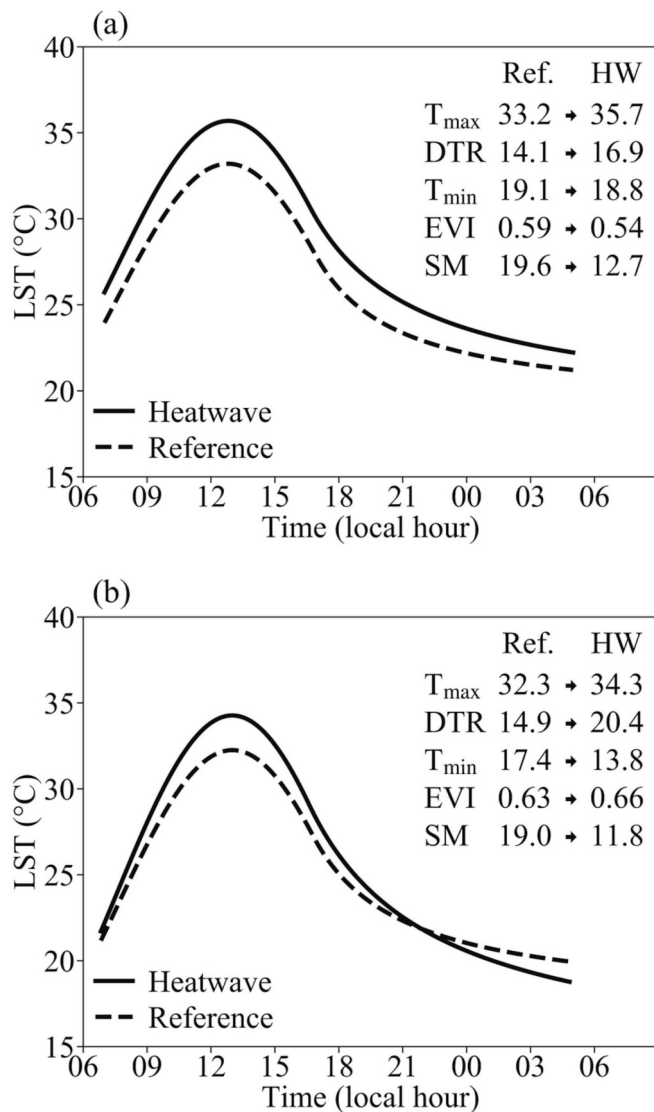
Fig. 11. Diurnal changes of LST represented by mean values of DTC parameters (indicated in the upper right corner) obtained from Himawari-8 LSTs in regions with large positive anomalies in T_{max} and *DTR* and negative anomalies in SM in Figs. 8. (a) Regions where EVI decreased (126.7°E–127.2°E, 35.6°N–36.1°N). (b) Regions where EVI did not decrease (139.3°E–139.8°E, 37.1°N–37.6°N). The dashed- and solid lines indicate the time-series LSTs represented by the mean composite values for the reference (Ref. in the upper right corner) and for the 2018 heatwave (HW in the upper right corner), respectively. Reference values are the mean LSTs for 2015–2021 except 2018.

not decrease (Fig. 11b), nighttime cooling was more pronounced than daytime heating, leading to a nighttime LST that was lower than the reference value during the heat wave. The deviations of *DTR* and T_{min} from the reference values were + 5.5 °C and − 3.6 °C, respectively, while T_{max} exhibited the smallest variation of +2.0 °C.

4. Discussion

4.1. Physical meaning of temperature-related DTC parameters

T_0, T_{min}, and T_{max} represent temperature levels caused by solar radiation, atmospheric conditions, elevation, and land cover. The spatial distributions corresponding to elevation and land cover (Fig. 1), and correlations with VIs or LE (Fig. 7) are well-known theoretically and statistically (Kogan, 1995; Gillies et al., 1997; Dousset et al., 2011). In

the current study, given that T_{min} is not directly impacted by solar radiation, it exhibited unique spatial distribution and correlations with environmental factors, compared with those of T_0 and T_{max} (Figs. 6 and 7). Although T_0 and T_{max} have similar spatial distributions, T_{max} can represent a more extreme thermal environment experienced by plants. Besides, the time required to reach T_{max}, t_m, varied depending on the topography and land cover. In fact, t_m in inland and coastal areas differed by over one hour (Fig. 6f). T_{max} considers such differences in diurnal cycle peaks between pixels; therefore, its spatial distribution is a purer representation of the temperature level of land surface properties than that of a satellite image snapshot.

DTR, T_a, and δT represent the diurnal changes strongly affected by thermal inertia of the land surface. This was supported by the observed correlations with daily EF in the site-based analysis (Table 3), as well as correlations with SM (Figs. 7 and 9) in the spatial and temporal analyses. Moreover, the *DTR* and δT anomalies caused by the heat wave corresponded with SM and LE/PLE anomalies (Figs. 8, S3, and S4). Thermal inertia decreases as SM decreases, and LST becomes more variable (increase in T_a, $-\delta T$, and *DTR*). A similar interpretation could be made for the relationships between EF and LE/PLE, which indirectly reflect SM content.

T_0 and T_a strongly reflect the response of the surface thermal properties induced by solar radiation, whereas δT reflects that induced by meteorological factors, such as wind and air-temperature. NDVI and EVI correlation coefficients of δT, *DTR*, and T_{min} were low (Fig. 7), which agrees with previous work showing weak correlation between *DTR* with NDVI in Europe (Duan et al., 2014). These weak correlations were likely due to differences in the time of observation (i.e., VIs were at daytime whereas temperature changes during nighttime). The same can also be said for the correlation coefficients for LE and LE/PLE, as the estimates were based on daytime observations (Mu et al., 2011). Moreover, T_a and $-\delta T$ tended to be smaller on the northern side of the mountains in Japan (Figs. 1b and 6b, c), which might be attributed to the reduction of solar radiation due to topography. Another possibility is that T_a and $-\delta T$ were smaller in complex terrains and coastal areas due to larger heat transfer to the atmosphere by mountain-valley and sea-land breeze circulations.

4.2. Which DTC parameters are useful for vegetation monitoring?

The site-based and satellite-based analyses revealed that T_{max} and *DTR* are the most useful parameters for monitoring vegetation from the perspective of sensitivity to geometric conditions, stability in model fitting, and correlations with other environmental factors. Theoretically, all DTC parameters can reflect solar radiation, atmospheric conditions, and surface thermal properties (Ignatov and Gutman, 1999; Li et al., 2013). Although previous studies have predicted a relationship between t_m, t_s, and k values and thermal inertia (Göttsche and Olesen, 2001; Duan et al., 2014), in the current study focusing on a humid climate region, the t_m, t_s, and k values obtained from Himawari-8 LSTs were more sensitive to topographic slope and geometric conditions than thermal properties (Fig. 6). T_0, T_a, and δT exhibited correlations with VIs and SM, respectively, implying that they can behave as thermal property-like parameters (Fig. 7). However, their values obtained in the fitting varied based on the calculation method of ω (Figs. 4 and S1). While T_{min} was robust to ω, its correlation with environmental factors was weaker than that of T_{max} and *DTR*. Hence, when focusing on the thermal environment at night, T_{min} is more appropriate than T_{max}.

DTR has a higher sensitivity than spectral VIs for detecting a drying signal. Comparison of the *DTR* anomaly with the EVI, NDVI, and SM anomalies during the heat wave (Figs. 8, S3, and S4) indicated that these parameters were able to detect drying signals that were undetectable by EVI and NDVI. These parameters reflect changes in the thermal inertia due to drying, whereas the VIs reflect visible damage, such as leaf reduction, leaf wilting, and plant death. Considering that visible damage occurs after hot and dry stresses, these parameters might be effective in earlier detection of drying signals. The fact that a large positive T_{max}

anomaly ($> 3.0\ °C$) corresponded well with the negative EVI anomaly (Fig. 8a and d) implies that there is visible vegetation damage. The difference between the DTC parameters and VIs observed in this study could also be due to differences in temporal resolution. However, the effect appears to have been small as LE/PLE, with the same temporal resolution as NDVI and EVI, showed anomalies suggesting drying (Fig. 8e), and the analysis period was sufficiently long (approximately three weeks).

As Indeed, the T_{max} and DTR obtained from Himawari-8 LSTs can provide more detailed detection of drying and water stress than spectral VIs, thereby contributing to the early detection of heat injury in plants and forest fires. Further normalization using a DTC parameter as in the Temperature Condition Index (TCI; Kogan, 1995) is expected to provide a more accurate drought index than the conventional indices using temperature information. Although a TCI-like index requires data accumulation over several years, Himawari-8/9 can meet this requirement in the near future. In fact, it is theoretically possible to calculate DTR-like values using day and night LSTs from polar-orbiting satellite sensors, such as VIIRS and MODIS. However, the uncertainty of DTR-like values obtained from LSTs with only two-time points would be large in warm and humid climatic regions such as East Asia due to the high cloud cover (Miura et al., 2019).

The weak negative correlations of t_m and t_s with SM (Fig. 7) is a contradictory trend in terms of thermal inertia. Theoretically, as SM decreases, the DTC phase should become earlier due to a decrease in thermal inertia. This contradiction can be attributed to the fact that t_m and t_s are more sensitive to topographic slope than to surface thermal inertia. For instance, t_m and t_s tend to be slower on open south-facing slopes, which experience longer daylight hours, than on north-facing slopes (Figs. 1b and 6). Hence, fitting the DTC model to the longer daylight hours (i.e., a longer half-period of the cosine term) would have slowed t_m and t_s. Moreover, the temporal correlation analysis (Fig. S5d–f), as well as time series variations on a shorter scale (Fig. S6c), did not identify correlations with thermal inertia.

Time-related parameters are difficult to use to detect drying signals. However, they provide information on the unique angular anisotropy of the Himawari-8 LSTs. Therefore, the time-related parameters have potential applications in the angular correction of LSTs for assimilation into meteorological and land surface models (Vinnikov et al., 2012; Chen et al., 2021).

4.3. Climate-induced differences in the drying detection

DTC parameters exhibited the expected performance in drying detection under drier climate conditions. T_{max} and DTR correlated higher with LE and EF at the ASM and CLP sites in Australia, which receive less precipitation than the four humid sites in the East Asia (Fig. 12 a–d). The tendency for T_{max} and DTR to be higher in drier conditions was supported by significant negative correlations with SM (Fig. S7). These correlations were strongest at the ASM site, which has a semi-arid climate. T_{min} did not significantly correlate with LE and EF even at the ASM site. Besides, t_m and t_s were also positively correlated with LE, EF, and SM at the ASM and CLP sites (Figs. S7 and S8). These relationships indicate a tendency for the phase to be slower in wetter conditions, which can be interpreted in terms of thermal inertia.

T_{max} and DTR are valuable indicators for detecting drying in both humid and semi-arid climates, although the responses of LE and LST to drying vary depending on the climatic conditions. The correlation coefficients of T_{max} and DTR with LE at the ASM and CLP sites (Fig. 12a and b) were opposite signs to those at the four humid sites (Table 3). When subjected to an atmospheric demand of drying conditions, a vegetation surface with abundant water content has a higher LE, whereas a vegetation surface with low water content has a lower LE (Wilson et al., 2002; Ács, 2003). Furthermore, vegetation with high moisture content has less variability in LST. The variations in T_{max} and DTR at the four humid sites were $< 10\ °C$ (Figs. 4 and 5), whereas those at the ASM and

CLP sites reached ~$20\ °C$ (Fig. 12). Besides, the correlations of T_{max} with LE (-0.80) and EF (-0.76) at the ASM site were greater than those of DTR (LE: -0.68, EF: 0.64). At the CRK, GCK, GDK, and CLP sites, correlations of DTR were greater than those of T_{max}. In conclusion, for vegetation monitoring across different climatic conditions, the use of both T_{max} and DTR would be necessary.

Decreases in GPP due to extreme temperatures and dryness might also potentially be detected by T_{max} and DTR. The negative correlations of T_{max} and DTR with daily GPP were highest at the ASM site with -0.67 and -0.49, respectively (Fig. 12e). The well correspondence between diurnal LST changes and GPP would be due to the common occurrence of vegetation water stress under semi-arid climates (Xiao et al., 2021). Significant correlations were also observed at the GCK and CLP sites (Table 3, Figs. 5e and 12f), and even at the CRK and TKY sites, anomalously high DTR corresponded to a midday depression of GPP. The midday depression did not appear to significantly impact the daily integrated GPP in humid climates, however, it is possible to detect midday depression of GPP by using an appropriate threshold for DTR.

4.4. Potential limitations associated with evaluation of DTC parameters

The observed higher correlations between T_{max} and DTR with other environmental factors, compared with those between T_0, T_a, and δT with environmental factors (Fig. 7) might be due to technical issues associated with fitting. The DTC model can experience difficulty in estimating T_0 in some cases (Duan et al., 2012; Hong et al., 2018; Chang et al., 2020); for example, underestimation of T_0 propagates to overestimation of T_a and δT (e.g., around $40°$ N, $140°$ E, and $40°$ N, $125°$ E, as shown in Fig. S3a and S3b). Meanwhile, the effects on T_{max} and DTR are small as the under- and over estimation of each parameter cancel each other out. Other possible factors include the effect of the biases in t_m and t_s on T_a and δT.

A more suitable solution for T_{max} and DTR might be obtained by treating ω as a free parameter instead of deriving it from Eq. (5). Duan et al. (2012) reported that treating ω as a free parameter improves the fitting accuracy. However, they also note that the physical meanings of the DTC parameters may be compromised as a result. There is a possibility of overestimating or underestimating ω in order to fit a distorted diurnal LST waveform containing noise and missing data, propagating the error to other DTC parameters. However, T_{max} and DTR were found to be robust to errors in T_0, T_a, and δT. If only T_{max} and DTR are used for vegetation monitoring, the drawbacks of using ω as a free parameter can be accepted.

Unlike SM, EF and LE/PLE do not always act as indicators of vegetation or soil moisture conditions. The significant negative correlations of DTR with EF at the CRK-, GCK-, and GDK- sites (Table 1) indicate a certain usefulness of DTR in monitoring drying, however, the opposite correlation was observed at the TKY site. The region around the TKY site during this season has abundant soil moisture due to the aftermath of the rainy season (so-called Baiu period), while mesoscale dry wind (so-called foehn wind) frequently blows on clear-sky days (Takane et al., 2017). The atmospheric demand from the foehn wind enhances energy, which is partitioned into latent heat fluxes (i.e., higher EF). Similar phenomenon may be seen in other humid regions. Indeed, many regions throughout Japan and the Korean Peninsula have reference LE/PLE > 0.6. Therefore, a positive anomaly in LE/PLE due to high atmospheric demand might indicate a decrease in the SM.

4.5. Influences of the heat wave on terrestrial vegetation

The positive anomalies in T_{max} and DTR were likely related to heating and drying caused by the heat wave, respectively (Fig. 8). The enhanced solar radiation heats the land surface, resulting in increased T_0 and T_a. This would account for the correspondence between the spatial distributions of the Double-High and positive anomaly of T_{max} (Fig. 2 and 8a). Drying of the land surface decreases the thermal inertia,
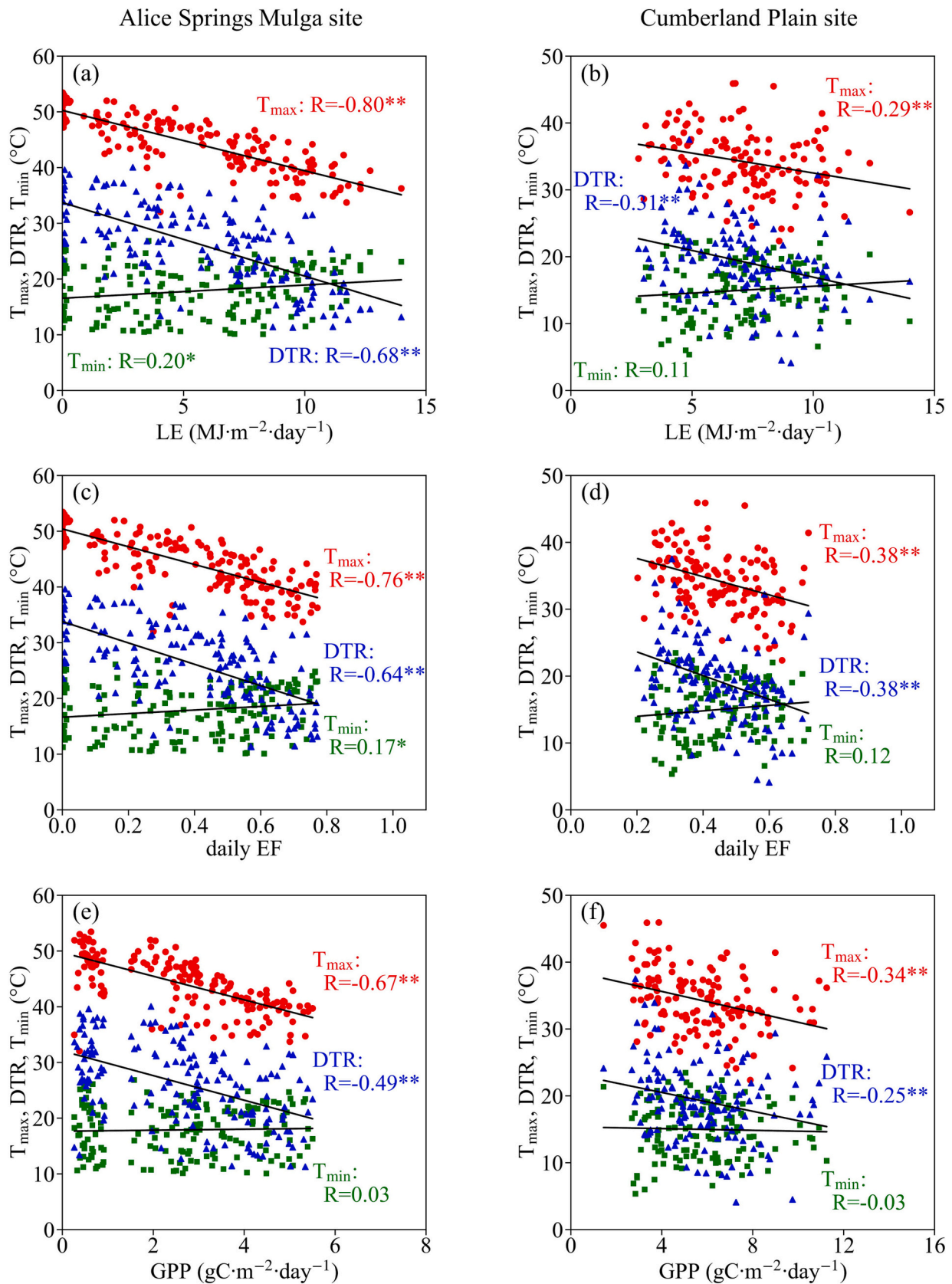
Fig. 12. T_{max}, DTR, and T_{min} versus daily LE (a, b), daily EF (c, d), and daily GPP (e, f) during summer at the Alice Spring Mulga site (left column) and the Cumberland Plain site (right column) in Australia. Red circles, blue triangles, and green squares are the results of T_{max}, DTR, and T_{min}, respectively. Correlation coefficients (R) are shown in the figures. Significance of correlation are indicated by superscript ** for $P < 0.01$ and * for $0.01 \leq P < 0.05$. The period is January–February in 2015–2021. (For interpretation of the references to colour in this figure legend, the reader is referred to the web version of this article.)

resulting in increased T_a and decreased δT. This would account for the relationship between the spatial distributions of the positive anomaly of DTR and the negative anomaly of SM (Fig. 8c and f). The smaller anomaly of DTR in the urban area might be due to the low moisture content of man-made surfaces in the urban area (Fig. 10a).

This heat wave caused drying and weak heating that had little effect on vegetation activity in Japan. However, anomalies of T_{max} (> +3 °C), DTR (> +4 °C), and EVI (< −0.04) around the Korean Peninsula indicated heating, drying, and a reduction in vegetation activity, respectively (Fig. 8a, c, and d). In contrast, the anomalies of T_{max} and EVI were smaller in Japan, although the same degree of drying occurred in the Korean Peninsula and Japan (Fig. 8c and f). The relationship among temperature levels, temperature increase during the day and temperature reduction during the night potentially detects drying that spectral VIs cannot detect (see differences between Fig. 11a and b). Furthermore, EVI might be more suitable than NDVI to detect reductions in vegetation activity around Japan and the Korean Peninsula where vegetation is abundant enough to saturate NDVI (Fig. S2a).

Although this heat wave was unprecedented for East Asia (Shimpo et al., 2019), the damage to terrestrial vegetation was minor compared to heat waves that have occurred in other regions. For example, the 2018 European heat wave in the same period and the Australian heat wave in December 2019 to January 2020 reported LST anomalies of above 10 °C over a wide area (EUMETSAT, 2019; Xiao et al., 2021). Meanwhile, in the East Asia heat wave, anomalies above 10 °C were rare (Fig. 10b). In addition, no large-scale forest fires were reported. The small damage to vegetation in East Asia by the heat wave was likely attributed to the rainy season (so-called Baiu period) that preceded the onset of summer. Shimpo et al. (2019) reported that a stationary Baiu front from early to mid-July in 2018 caused record-breaking heavy rainfall events, especially in Japan. The vegetation retained sufficient water content during this extreme rainy season, so that it may have avoided drought even though drying occurred during the subsequent heat wave.

5. Conclusion

This study examined DTC parameters from in situ LSTs and from Himawari-8 LSTs to establish the applicability of DTC parameters for the detection of vegetation drying under humid climates. First, DTC parameters from in situ LSTs free from missing data observed at the vegetation sites were examined. Significant correlations between T_a, T_{max}, and DTR with daily LE, as well as between T_a and DTR with daily EF, were observed. Moreover, T_0, T_a, and δT were strongly dependent on the ω calculation method. Subsequent comparison of DTC parameters from the Himawari-8 LSTs with EVI, NDVI, LE, LE/PLE, and SM revealed that spatial distribution of the reference T_{max} had the highest correlation coefficients with those of VIs, LE, and LE/PLE, whereas the spatial distribution of the reference DTR had the highest correlation coefficient with that of SM. The spatial distribution of the DTR anomaly during the heat wave corresponded well with the drying signals indicated as negative SM anomalies. Regions with large positive anomalies of both T_{max} and DTR corresponded to negative EVI anomalies, indicating visible vegetation damage. Moreover, temporal correlation analysis showed that T_{max} and DTR had consistent negative correlations with SM across the study area.

Collectively, our analysis revealed that T_{max} and DTR are the most useful for vegetation monitoring in terms of sensitivity to geometric conditions, robustness to ω, and correlations with EF, VIs, and SM. Furthermore, the combination of T_{max} and DTR potentially detects drying- and heat-related vegetation stresses not detectable by spectral VIs. Additionally, correlations between DTC parameters and VIs and SM were quantitatively established under more realistic conditions, including short-term missing data and noise, as compared to previous qualitative reports (Göttsche and Olesen, 2001; Duan et al., 2014; Hong

et al., 2018). Contrary to the expectations of previous studies, time-related parameters (t_m, t_s, and k) were found to be sensitive to topographic slope and geometric conditions, thus impeding their application to vegetation monitoring. At sites with greater LE and LST responses to drying, time-related parameters also correlated significantly with LE, EF, and SM. Detecting signals of vegetation drying in humid climates is more challenging compared to semi-arid climates. Nevertheless, T_{max} and DTR have been demonstrated to be useful even in such humid environments.

The frequency of extreme heat events in East Asia is expected to increase with progression of global warming (Imada et al., 2018; Imada et al., 2019). The Korean Peninsula also faces frequent forest fires during the dry period in early spring (Kang et al., 2020). Hence, T_{max}, and DTR from Himawari-8/9 LSTs might prove useful for monitoring heating, drying, and water stress in such future extreme heat and dry events. Several studies have demonstrated that NIRvP, product of near-infrared reflectance of vegetation and photosynthetically active radiation (Badgley et al., 2019), is a strong predictor in estimating GPP using geostationary satellite data (Khan et al., 2021; Jeong et al., 2023). Nevertheless, the NIRvP-based GPP estimations does not have a capability to incorporate diurnal stress effects. Utilizing DTR as a metric for stress detection would be a good constraint to downregulate the NIRvP-based GPP on a diurnal scale. Moreover, T_{max}, and DTR have potential application for the detection of smaller spatial scale signals, such as high temperature injury of crops, and drought detection in arid/semi-arid regions, such as Australia. However, to confirm these findings and make them more widely applicable, similar analyses are warranted in additional sites over a larger geographical area.

CRediT authorship contribution statement

Yuhei Yamamoto: Conceptualization, Methodology, Software, Validation, Formal analysis, Investigation, Resources, Data curation, Writing – original draft, Writing – review & editing, Visualization, Funding acquisition. **Kazuhito Ichii:** Data curation, Writing – review & editing, Supervision, Project administration, Funding acquisition. **Youngryel Ryu:** Resources, Data curation, Writing – review & editing. **Minseok Kang:** Resources, Data curation, Writing – review & editing. **Shohei Murayama:** Resources, Data curation, Writing – review & editing, Funding acquisition. **Su-Jin Kim:** Resources, Data curation, Funding acquisition. **Jamie R. Cleverly:** Resources, Data curation, Writing – review & editing.

Declaration of Competing Interest

None.

Data availability

Data will be made available on request.

Acknowledgments

Appendix A. Supplementary data

Supplementary data to this article can be found online at https://doi.org/10.1016/j.rse.2023.113572.

References

Ács, F., 2003. A comparative analysis of transpiration and bare soil evaporation. Bound. Layer Meteorol. 109, 139–162.

Aires, F., Prigent, C., Rossow, W.B., 2004. Temporal interpolation of global surface skin temperature diurnal cycle over land under clear and cloudy conditions. J. Geophys. Res. 109, D04313. https://doi.org/10.1029/2003JD003527.

Albergel, C., Dutra, E., Bonan, B., Zheng, Y., Munier, S., Balsamo, G., de Rosnay, P., Muñoz-Sabater, J., Calvet, J.-C., 2019. Monitoring and forecasting the impact of the 2018 summer heatwave on vegetation. Remote Sens. 11, 520. https://doi.org/10.3390/rs11050520.

Badgley, G., Anderegg, L.D.L., Berry, J.A., Field, C.B., 2019. Terrestrial gross primary production: using NIRV to scale from site to globe. Glob. Chang. Biol. 25, 3731–3740. https://doi.org/10.1111/gcb.14729.

Beck, H.E., Zimmermann, N.E., McVicar, T.R., Vergopolan, N., Berg, A., Wood, E.F., 2018. Present and future Köppen-Geiger climate classification maps at 1-km resolution. Sci. Data 5, 180214. https://doi.org/10.1038/sdata.2018.214.

Bessho, K., Date, K., Hayashi, M., Ikeda, A., Imai, T., Inoue, H., Kumagai, Y., Miyakawa, T., Murata, H., Ohno, T., Okuyama, A., Oyama, R., Sasaki, Y., Shimazu, Y., Shimoji, K., Sumida, Y., Suzuki, M., Taniguchi, H., Tsuchiyama, H., Uesawa, D., Yokota, H., Yoshida, R., 2016. An introduction to Himawari-8/9 — Japan's new-generation geostationary meteorological satellites. J. Meteorol. Soc. Jpn. Ser. II 94, 151–183. https://doi.org/10.2151/jmsj.2016-009.

Chang, Y., Ding, Y., Zhao, Q., Zhang, S., 2020. A comprehensive evaluation of 4-parameter diurnal temperature cycle models with in situ and MODIS LST over alpine meadows in the tibetan plateau. Remote Sens. 12, 103. https://doi.org/10.3390/RS12010103.

Chang, Y., Xiao, J., Li, Xuxiang, Frolking, S., Zhou, D., Schneider, A., Weng, Q., Yu, P., Wang, X., Li, X., Liu, S., Wu, Y., 2021. Exploring diurnal cycles of surface urban heat island intensity in Boston with land surface temperature data derived from GOES-R geostationary satellites. Sci. Total Environ. 763, 144224 https://doi.org/10.1016/j.scitotenv.2020.144224.

Chen, W., Pinker, R.T., Ma, Y., Hulley, G., Borbas, E., Islam, T., Cawse-Nicholson, K.-A., Hook, S., Hain, C., Basara, J., 2021. Land surface temperature from GOES-east and GOES-west. J. Atmos. Ocean. Technol. 38, 843–858. https://doi.org/10.1175/JTECH-D-20-0086.1.

Cheng, J., Liang, S., Yao, Y., Zhang, X., 2013. Estimating the optimal broadband emissivity spectral range for calculating surface longwave net radiation. IEEE Geosci. Remote Sens. Lett. 10, 401–405. https://doi.org/10.1109/LGRS.2012.2206367.

Damm, A., Elbers, J., Erler, A., Gioli, B., Hamdi, K., Hutjes, R., Kosvancova, M., Meroni, M., Miglietta, F., Moersch, A., Moreno, J., Schickling, A., Sonnenschein, R., Udelhoven, T., van der Linden, S., Hostert, P., Rascher, U., 2010. Remote sensing of sun-induced fluorescence to improve modeling of diurnal courses of gross primary production (GPP). Glob. Chang. Biol. 16, 171–186. https://doi.org/10.1111/j.1365-2486.2009.01908.x.

Didan, K., Barreto, A., 2018. VIIRS/NPP vegetation indices 16-day L3 global 500m SIN grid V001 [Data set]. NASA EOSDIS Land Process. DAAC. https://doi.org/10.5067/VIIRS/VNP13A1.001 (accessed 4 July 2022).

Dousset, B., Gourmelon, F., Laaidi, K., Zeghnoun, A., Giraudet, E., Bretin, P., Mauri, E., Vandentorren, S., 2011. Satellite monitoring of summer heat waves in the Paris metropolitan area. Int. J. Climatol. 31, 313–323. https://doi.org/10.1002/joc.2222.

Duan, S.-B., Li, Z.-L., Tang, B.-H., Wu, H., Tang, R., 2014. Direct estimation of land-surface diurnal temperature cycle model parameters from MSG-SEVIRI brightness temperatures under clear sky conditions. Remote Sens. Environ. 150, 34–43. https://doi.org/10.1016/j.rse.2014.04.017.

Duan, S.-B., Li, Z.-L., Wang, N., Wu, H., Tang, B.-H., 2012. Evaluation of six land-surface diurnal temperature cycle models using clear-sky in situ and satellite data. Remote Sens. Environ. 124, 15–25. https://doi.org/10.1016/j.rse.2012.04.016.

Duan, S.-B., Li, Z.-L., Wu, H., Tang, B.-H., Jiang, X., Zhou, G., 2013. Modeling of day-to-day temporal progression of clear-sky land surface temperature. IEEE Geosci. Remote Sens. Lett. 10, 1050–1054. https://doi.org/10.1109/LGRS.2012.2228465.

Enomoto, T., Hoskins, B.J., Matsuda, Y., 2003. The formation mechanism of the bonin high in august. Q. J. R. Meteorol. Soc. 129, 157–178. https://doi.org/10.1256/qj.01.211.

Farr, T.G., Kobrick, M., 2000. Shuttle radar topography mission produces a wealth of data. Eos Trans. AGU 81, 583–585. https://doi.org/10.1029/EO081i048p00583.

Farr, T.G., Rosen, P.A., Caro, E., Crippen, R., Duren, R., Hensley, S., Kobrick, M., Paller, M., Rodriguez, E., Roth, L., Seal, D., Shaffer, S., Shimada, J., Umland, J., Werner, M., Oskin, M., Burbank, D., Alsdorf, D., 2007. The shuttle radar topography mission. Rev. Geophys. 45, RG2004. https://doi.org/10.1029/2005RG000183.

Fisher, J.B., Lee, B., Purdy, A.J., Halverson, G.H., Dohlen, M.B., Cawse-Nicholson, K., Wang, A., Anderson, R.G., Aragon, B., Arain, M.A., Baldocchi, D.D., Baker, J.M., Barral, H., Bernacchi, C.J., Bernhofer, C., Biraud, S.C., Bohrer, G., Brunsell, N., Cappelaere, B., Castro-Contreras, S., Chun, J., Conrad, B.J., Cremonese, E., Demarty, J., Desai, A.R., De Ligne, A., Foltýnová, L., Goulden, M.L., Griffis, T.J., Grünwald, T., Johnson, M.S., Kang, M., Kelbe, D., Kowalska, N., Lim, J.-H., Maïnassara, I., McCabe, M.F., Missik, J.E.C., Mohanty, B.P., Moore, C.E., Morillas, L., Morrison, R., Munger, J.W., Posse, G., Richardson, A.D., Russell, E.S., Ryu, Y., Sanchez-Azofeifa, A., Schmidt, M., Schwartz, E., Sharp, I., Šigut, L., Tang, Y., Hulley, G., Anderson, M., Hain, C., French, A., Wood, E., Hook, S., 2020. ECOSTRESS: NASA's next generation mission to measure evapotranspiration from the international space station. Water Resour. Res. 56, e2019WR026058 https://doi.org/10.1029/2019WR026058.

Gillies, R.R., Kustas, W.P., Humes, K.S., 1997. A verification of the 'triangle' method for obtaining surface soil water content and energy fluxes from remote measurements of the normalized difference vegetation index (NDVI) and surface e. Int. J. Remote Sens. 18, 3145–3166. https://doi.org/10.1080/014311697217026.

Göttsche, F.-M., Olesen, F.-S., 2009. Modelling the effect of optical thickness on diurnal cycles of land surface temperature. Remote Sens. Environ. 113, 2306–2316. https://doi.org/10.1016/j.rse.2009.06.006.

Göttsche, F.-M., Olesen, F.-S., 2001. Modelling of diurnal cycles of brightness temperature extracted from METEOSAT data. Remote Sens. Environ. 76, 337–348. https://doi.org/10.1016/S0034-4257(00)00214-5.

Green, J.K., Ballantyne, A., Abramoff, R., Gentine, P., Makowski, D., Ciais, P., 2022. Surface temperatures reveal patterns of vegetation water stress and their environmental drivers across the tropical americas. Glob. Chang. Biol. 28, 2940–2955. https://doi.org/10.1111/gcb.16139.

Hong, F., Zhan, W., Göttsche, F.-M., Liu, Z., Zhou, J., Huang, F., Lai, J., Li, M., 2018. Comprehensive assessment of four-parameter diurnal land surface temperature cycle models under clear-sky. ISPRS J. Photogramm. Remote Sens. 142, 190–204. https://doi.org/10.1016/j.isprsjprs.2018.06.008.

Hulley, G.C., Hook, S.J., Abbott, E., Malakar, N., Islam, T., Abrams, M., 2015. The ASTER global emissivity dataset (ASTER GED): mapping Earth's emissivity at 100 meter spatial scale. Geophys. Res. Lett. 42, 7966–7976. https://doi.org/10.1002/2015GL065564.

Hwang, Y., Ryu, Y., Huang, Y., Kim, J., Iwata, H., Kang, M., 2020. Comprehensive assessments of carbon dynamics in an intermittently-irrigated rice paddy. Agric. For. Meteorol. 285–286, 107933 https://doi.org/10.1016/j.agrformet.2020.107933.

Ignatov, A., Gutman, G., 1999. Monthly mean diurnal cycles in surface temperatures over land for global climate studies. J. Clim. 12, 1900–1910. https://doi.org/10.1175/1520-0442(1999)012<1900:MMDCIS>2.0.CO;2.

Imada, Y., Shiogama, H., Takahashi, C., Watanabe, M., Mori, M., Kamae, Y., Maeda, S., 2018. Climate change increased the likelihood of the 2016 heat extremes in Asia. Bull. Am. Meteorol. Soc. 99, S97–S101. https://doi.org/10.1175/bams-d-17-0109.1.

Imada, Y., Watanabe, M., Kawase, H., Shiogama, H., Arai, M., 2019. The july 2018 high temperature event in Japan could not have happened without human-induced global warming. Sola 15A, 8–12. https://doi.org/10.2151/sola.15a-002.

Inamdar, A.K., French, A., Hook, S., Vaughan, G., Luckett, W., 2008. Land surface temperature retrieval at high spatial and temporal resolutions over the southwestern United States. J. Geophys. Res. 113, D07107. https://doi.org/10.1029/2007JD009048.

Japanese Ministry of Health, Labour and Welfare, 2021. The vital statistics in Japan (September 2021), article written in Japanese. https://www.mhlw.go.jp/toukei/saikin/hw/jinkou/geppo/m2021/dl/all0309.pdf.

Jeong, S., Ryu, Y., Dechant, B., Liu, J., Li, B., Li, X., 2023. Tracking diurnal to seasonal variations of gross primary productivity using a geostationary satellite, GK-2A advanced meteorological imager in korean peninsula. Remote Sens. Environ. 284, 113365 https://doi.org/10.1016/j.rse.2022.113365.

Jiang, Y., Fu, P., Weng, Q., 2015. Downscaling GOES land surface temperature for assessing heat wave health risks. IEEE Geosci. Remote Sens. Lett. 12, 1605–1609. https://doi.org/10.1109/LGRS.2015.2414897.

Kang, M., Ruddell, B.L., Cho, C., Chun, J., Kim, J., 2017. Identifying CO2 advection on a hill slope using information flow. Agric. For. Meteorol. 232, 265–278. https://doi.org/10.1016/j.agrformet.2016.08.003.

Kang, Y., Jang, E., Im, J., Kwon, C., Kim, S., 2020. Developing a new hourly forest fire risk index based on catboost in South Korea. Appl. Sci. 10, 8213. https://doi.org/10.3390/app10228213.

Khan, A.M., Stoy, P.C., Douglas, J.T., Anderson, M., Diak, G., Otkin, J.A., Hain, C., Rehbein, E.M., McCorkel, J., 2021. Reviews and syntheses: ongoing and emerging opportunities to improve environmental science using observations from the advanced baseline imager on the geostationary operational environmental satellites. Biogeosciences 18, 4117–4141. https://doi.org/10.5194/bg-18-4117-2021.

Kogan, F.N., 1995. Application of vegetation index and brightness temperature for drought detection. Adv. Space Res. 15, 91–100. https://doi.org/10.1016/0273-1177(95)00079-T.

Konrad, W., Katul, G., Roth-Nebelsick, A., 2021. Leaf temperature and its dependence on atmospheric CO2 and leaf size. Geol. J. 56, 866–885. https://doi.org/10.1002/gj.3757.

Kosaka, Y., Nakamura, H., 2010. Mechanisms of meridional teleconnection observed between a summer monsoon system and a subtropical anticyclone. Part I: the Pacific-Japan pattern. J. Clim. 23, 5085–5108. https://doi.org/10.1175/2010JCLI3413.1.

Kosaka, Y., Nakamura, H., Watanabe, M., Kimoto, M., 2009. Analysis on the dynamics of a wave-like teleconnection pattern along the summertime Asian jet based on a reanalysis dataset and climate model simulations. J. Meteorol. Soc. Jpn. 87, 561–580. https://doi.org/10.2151/jmsj.87.561.

Li, Z.-L., Tang, B.-H., Wu, H., Ren, H., Yan, G., Wan, Z., Trigo, I.F., Sobrino, J.A., 2013. Satellite-derived land surface temperature: current status and perspectives. Remote Sens. Environ. 131, 14–37. https://doi.org/10.1016/j.rse.2012.12.008.

Liu, L., Guan, L., Liu, X., 2017. Directly estimating diurnal changes in GPP for C3 and C4 crops using far-red sun-induced chlorophyll fluorescence. Agric. For. Meteorol. 232, 1–9. https://doi.org/10.1016/j.agrformet.2016.06.014.

Lorenz, R., Davin, E.L., Lawrence, D.M., Stöckli, R., Seneviratne, S.I., 2013. How important is vegetation phenology for european climate and heat waves? J. Clim. 26, 10077–10100. https://doi.org/10.1175/JCLI-D-13-00040.1.

Miura, T., Nagai, S., Takeuchi, M., Ichii, K., Yoshioka, H., 2019. Improved characterisation of vegetation and land surface seasonal dynamics in Central Japan with Himawari-8 hypertemporal data. Sci. Rep. 9, 15692. https://doi.org/10.1038/s41598-019-52076-x.

Mladenova, I.E., Bolten, J.D., Crow, W., Sazib, N., Reynolds, C., 2020. Agricultural drought monitoring via the assimilation of SMAP soil moisture retrievals into a global soil water balance model. Front. Big Data 3, 10. https://doi.org/10.3389/fdata.2020.00010.

Mladenova, I.E., Bolten, J.D., Crow, W.T., Sazib, N., Cosh, M.H., Tucker, C.J., Reynolds, C., 2019. Evaluating the operational application of SMAP for global agricultural drought monitoring. IEEE J. Sel. Top. Appl. Earth Obs. Remote Sens. 12, 3387–3397. https://doi.org/10.1109/JSTARS.2019.2923555.

Mu, Q., Zhao, M., Running, S.W., 2011. Improvements to a MODIS global terrestrial evapotranspiration algorithm. Remote Sens. Environ. 115, 1781–1800. https://doi.org/10.1016/j.rse.2011.02.019.

Nitta, T., 1987. Convective activities in the tropical Western Pacific and their impact on the northern hemisphere summer circulation. J. Meteorol. Soc. Jpn. 65, 373–390. https://doi.org/10.2151/jmsj1965.65.3_373.

Pallas Jr., J.E., Michel, B.E., Harris, D.G., 1967. Photosynthesis, transpiration, leaf temperature, and stomatal activity of cotton plants under varying water potentials. Plant Physiol. 42, 76–88. https://doi.org/10.1104/pp.42.1.76.

Paul-Limoges, E., Damm, A., Hueni, A., Liebisch, F., Eugster, W., Schaepman, M.E., Buchmann, N., 2018. Effect of environmental conditions on sun-induced fluorescence in a mixed forest and a cropland. Remote Sens. Environ. 219, 310–323. https://doi.org/10.1016/j.rse.2018.10.018.

Qiu, B., Ge, J., Guo, W., Pitman, A.J., Mu, M., 2020. Responses of australian dryland vegetation to the 2019 heat wave at a subdaily scale. Geophys. Res. Lett. 47, 1–8. https://doi.org/10.1029/2019GL086569.

Quan, J., Chen, Y., Zhan, W., Wang, J., Voogt, J., Li, J., 2014. A hybrid method combining neighborhood information from satellite data with modeled diurnal temperature cycles over consecutive days. Remote Sens. Environ. 155, 257–274. https://doi.org/10.1016/j.rse.2014.08.034.

Saigusa, N., Yamamoto, S., Murayama, S., Kondo, H., 2005. Inter-annual variability of carbon budget components in an AsiaFlux forest site estimated by long-term flux measurements. Agric. For. Meteorol. 134, 4–16. https://doi.org/10.1016/j.agrformet.2005.08.016.

Saito, K., Fujita, T., Yamada, Y., Ishida, J.-I., Kumagai, Y., Aranami, K., Ohmori, S., Nagasawa, R., Kumagai, S., Muroi, C., Kato, T., Eito, H., Yamazaki, Y., 2006. The operational JMA nonhydrostatic mesoscale model. Mon. Weather Rev. 134, 1266–1298. https://doi.org/10.1175/MWR3120.1.

Saitoh, T.S., Shimada, T., Hoshi, H., 1996. Modeling and simulation of the Tokyo urban heat island. Atmos. Environ. 30, 3431–3442. https://doi.org/10.1016/1352-2310(95)00489-0.

Shimpo, A., Takemura, K., Wakamatsu, S., Togawa, H., Mochizuki, Y., Takekawa, M., Tanaka, S., Yamashita, K., Maeda, S., Kurora, R., Murai, H., Kitabatake, N., Tsuguti, H., Mukougawa, H., Iwasaki, T., Kawamura, R., Kimoto, M., Takayabu, I., Takayabu, Y.N., Tanimoto, Y., Hirooka, T., Masumoto, Y., Watanabe, M., Tsuboki, K., Nakamura, H., 2019. Primary factors behind the heavy rain event of july 2018 and the subsequent heat wave in Japan. Sola 15A, 13–18. https://doi.org/10.2151/sola.15a-003.

Sismanidis, P., Bechtel, B., Keramitsoglou, I., Kiranoudis, C.T., 2017. Mapping the spatiotemporal dynamics of Europe's land surface temperatures. IEEE Geosci. Remote Sens. Lett. 15, 202–206. https://doi.org/10.1109/LGRS.2017.2779829.

Skinner, C.B., Poulsen, C.J., Mankin, J.S., 2018. Amplification of heat extremes by plant CO2 physiological forcing. Nat. Commun. 9, 1094. https://doi.org/10.1038/s41467-018-03472-w.

Sulla-Menashe, D., Gray, J.M., Abercrombie, S.P., Friedl, M.A., 2019. Hierarchical mapping of annual global land cover 2001 to present: the MODIS collection 6 land cover product. Remote Sens. Environ. 222, 183–194. https://doi.org/10.1016/j.rse.2018.12.013.

Takane, Y., Kondo, H., Kusaka, H., Katagi, J., Nagafuchi, O., Nakazawa, K., Kaneyasu, N., Miyakami, Y., 2017. Foehnlike wind with a traditional foehn effect plus dry-diabatic heating from the ground surface contributing to high temperatures at the end of a leeward area. J. Appl. Meteorol. Climatol. 56, 2067–2079. https://doi.org/10.1175/JAMC-D-16-0257.1.

Takenaka, H., Sakashita, T., Higuchi, A., Nakajima, T., 2020. Geolocation correction for geostationary satellite observations by a phase-only correlation method using a visible channel. Remote Sens. 12, 2472. https://doi.org/10.3390/RS12152472.

Urban, J., Ingwers, M.W., McGuire, M.A., Teskey, R.O., 2017. Increase in leaf temperature opens stomata and decouples net photosynthesis from stomatal conductance in Pinus taeda and Populus deltoides x nigra. J. Exp. Bot. 68, 1757–1767. https://doi.org/10.1093/jxb/erx052.

Verstraeten, W.W., Veroustraete, F., Van Der Sande, C.J., Grootaers, I., Feyen, J., 2006. Soil moisture retrieval using thermal inertia, determined with visible and thermal spaceborne data, validated for european forests. Remote Sens. Environ. 101, 299–314. https://doi.org/10.1016/j.rse.2005.12.016.

Vinnikov, K.Y., Yu, Y., Goldberg, M.D., Tarpley, D., Romanov, P., Laszlo, I., Chen, M., 2012. Angular anisotropy of satellite observations of land surface temperature. Geophys. Res. Lett. 39, L23802. https://doi.org/10.1029/2012GL054059.

Wang, L., Guo, N., Wang, W., Zuo, H., 2019. Optimization of the local split-window algorithm for FY-4A land surface temperature retrieval. Remote Sens. 11, 2016. https://doi.org/10.3390/rs11172016.

Weng, Q., Fu, P., 2014. Modeling diurnal land temperature cycles over Los Angeles using downscaled GOES imagery. ISPRS J. Photogramm. Remote Sens. 97, 78–88. https://doi.org/10.1016/j.isprsjprs.2014.08.009.

Wilson, K.B., Baldocchi, D.D., Aubinet, M., Berbigier, P., Bernhofer, C., Dolman, H., Falge, E., Field, C., Goldstein, A., Granier, A., Grelle, A., Halldor, T., Hollinger, D., Katul, G., Law, B.E., Lindroth, A., Meyers, T., Moncrieff, J., Monson, R., Oechel, W., Tenhunen, J., Valentini, R., Verma, S., Vesala, T., Wofsy, S., 2002. Energy partitioning between latent and sensible heat flux during the warm season at FLUXNET sites. Water Resour. Res. 38, 301–3011. https://doi.org/10.1029/2001wr000989.

Xiao, J., Fisher, J.B., Hashimoto, H., Ichii, K., Parazoo, N.C., 2021. Emerging satellite observations for diurnal cycling of ecosystem processes. Nat. Plants 7, 877–887. https://doi.org/10.1038/s41477-021-00952-8.

Xu, H., Yu, Y., Tarpley, D., Gottsche, F.-M., Olesen, F.-S., 2014. Evaluation of GOES-R land surface temperature algorithm using SEVIRI satellite retrievals with in situ measurements. IEEE Trans. Geosci. Remote Sens. 52, 3812–3822. https://doi.org/10.1109/TGRS.2013.2276426.

Yamamoto, Y., Ichii, K., Higuchi, A., Takenaka, H., 2020. Geolocation accuracy assessment of Himawari-8/AHI imagery for application to terrestrial monitoring. Remote Sens. 12, 1372. https://doi.org/10.3390/RS12091372.

Yamamoto, Y., Ichii, K., Ryu, Y., Kang, M., Murayama, S., 2022. Uncertainty quantification in land surface temperature retrieved from Himawari-8/AHI data by operational algorithms. ISPRS J. Photogramm. Remote Sens. 191, 171–187. https://doi.org/10.1016/j.isprsjprs.2022.07.008.

Yamamoto, Y., Ishikawa, H., 2020. Influence of urban spatial configuration and sea breeze on land surface temperature on summer clear-sky days. Urban Clim. 31, 100578 https://doi.org/10.1016/j.uclim.2019.100578.

Yamamoto, Y., Ishikawa, H., 2018. Thermal land surface emissivity for retrieving land surface temperature from Himawari-8. J. Meteorol. Soc. Jpn. 96B, 43–58. https://doi.org/10.2151/jmsj.2018-004.

Yamamoto, Y., Ishikawa, H., Oku, Y., Hu, Z., 2018. An algorithm for land surface temperature retrieval using three thermal infrared bands of Himawari-8. J. Meteorol. Soc. Jpn. 96B, 59–76. https://doi.org/10.2151/jmsj.2018-005.

Yuan, W., Liu, S., Zhou, Guangsheng, Zhou, Guoyi, Tieszen, L.L., Baldocchi, D., Bernhofer, C., Gholz, H., Goldstein, A.H., Goulden, M.L., Hollinger, D.Y., Hu, Y., Law, B.E., Stoy, P.C., Vesala, T., Wofsy, S.C., 2007. Deriving a light use efficiency model from eddy covariance flux data for predicting daily gross primary production across biomes. Agric. For. Meteorol. 143, 189–207. https://doi.org/10.1016/j.agrformet.2006.12.001.

Zhou, S., Cheng, J., 2020. An improved temperature and emissivity separation algorithm for the advanced himawari imager. IEEE Trans. Geosci. Remote Sens. 58, 7105–7124. https://doi.org/10.1109/TGRS.2020.2979846.